PCCP

Progress and Perspective on the Reaction Mechanisms in Mild-acidic Aqueous Zinc–Manganese-Oxide Batteries

Journal:	*Physical Chemistry Chemical Physics*
Manuscript ID	CP-PER-04-2023-001843.R1
Article Type:	Perspective
Date Submitted by the Author:	15-Aug-2024

Complete List of Authors:	Bergschneider, Matthew; The University of Texas at Dallas, Department of Materials Science and Engineering Kong, Fantai; The University of Texas at Dallas, Materials Science & Engineering Kong, Fantai; Hunt Energy Enterprises, LLC Hwang, Taesoon; The University of Texas at Dallas, Department of Materials Science and Engineering Jo, Youhwan; The University of Texas at Dallas, Department of Materials Science and Engineering Alvarez, Denyce; Hunt Energy Enterprises, LLC Cho, Kyeongjae; The University of Texas at Dallas, Department of Materials Science and Engineering

ARTICLE

Progress and Perspective on the Reaction Mechanisms in Mild-acidic Aqueous Zinc–Manganese-Oxide Batteries

Received 00th January 20xx,
Accepted 00th January 20xx

DOI: 10.1039/x0xx00000x

Matthew Bergschneider,[a] Fantai Kong,[a,b] Taesoon Hwang,[a] Youhwan Jo,[a] Denyce Alvarez,[b] and Kyeongjae Cho [a]

The appeal of safe, energy-dense, and ecologically-sourced MnO_2 as cathode to rechargeable aqueous zinc−metal-oxide batteries (AZMOBs) has brought significant research power to bear, but unexpected complexities has resulted in a decade of confusion and conflicting claims. The literature base is near saturation with a mix of efforts to achieve practical, rechargeable Zn-ion batteries, and to untangle the presented electrochemical mechanisms. We have summarized the respective mechanisms and contextualize the respective justifications. As new perspectives arise from *in situ* and *operando* techniques, renewed efforts must solidify mechanistic understandings and reconcile disparate data through judicial application of *ab initio* modelling. In light of the variety of MnO_2 cathode phases and stable, meta-stable, and complex reaction products, this perspective stresses the need for greater supplementation of *in situ* and *operando* characterization with modelling, such as Density Functional Theory. Through the elucidation of key mechanisms in dynamic operating and characterization conditions, the body of previously contradictory research and routes to practical batteries may be unified, and guide the way to longevity and grid-scale applicable charge rate and capacity.

1. Introduction

With ever increasing demand for renewable energy across the globe, an imminent need for grid-scale energy storage calls for safe and reliable batteries. Affordable cathode materials with excellent capacity retention for long cycle life—under applicable charge/discharge rates—are essential to develop. Due to the natural abundance of Mn—the fifth most abundant metal in the earth's crust—as a low-toxicity metal-oxide cathode with Zn as a potentially viable metal anode, the added safety of aqueous electrolytes make rechargeable aqueous Zn-ion batteries are an intriguing solution. Among the Zn-MnO2 chemistries, the aqueous mild-acidic system with pH 4-6 has attracted a lot of attention recently due to lower corrosion, longer durability and lower manufacturing cost.

Even though in the past decade, numerous impressive progresses have been reported, Zn/MnO_2 batteries with mild-acidic aqueous electrolytes still yielded myriad challenges to understand the underlying reaction mechanism. This largely originates from the complex nature of manganese oxides which have many stable polymorphs. As illustrated in Fig. 1, MnO_2 may adopt crystal structures with one-dimensional 1 × 1, 2 × 1, 2 × 2, etc. tunnels or 2-D planes formed by interconnected $[MnO_6]$ octahedra.[1] Such features are believed to facilitate reversible ion insertion/extraction which was long presumed to be the primary contribution to electrochemical capacity. However, recent research efforts have uncovered more complex working mechanisms and side reactions within the battery systems using advanced *in situ* and *operando* characterization techniques. These findings highlight inconsistencies within the extensive body of *ex situ* characterization literature, necessitating clarification through *in situ* methods and robust theoretical frameworks. For example, literature of one popular phase, α-MnO_2—featuring both 1 × 1 and 2 × 2 one-dimensional tunnels—exhibits conflicting reports claiming a variety of mechanisms.[2–6] These mechanisms range from complete but reversible transformation to a new phase—or developing broken-tunnel or planar features—during discharge/charge, to that proton (H^+) intercalation, followed by kinetically slower Zn^{2+}. Many obfuscating factors rise from "side reactions" consuming Zn^{2+}, anions, and OH^- constituents of the aqueous electrolyte at the cathode—and Zn metal anode—surface. To isolate and identify given mechanisms or side reactions, studies have contrasted electrolyte compositions with alternative salts such as $Zn(CH_3OOH)_2$ and $MnSO_4$ additives.

Elucidating the fundamental electrochemical mechanisms and differentiating between benign, parasitic, and degrading reactions are crucial steps to better guide experimental efforts. This approach aims to optimize specific energy capacity and cycle life, making rechargeable Zn/MnO_2 batteries a more viable option. In this article, we focus on a review of the phases and reaction mechanisms of the manganese oxide cathode, and provide a perspective on unifying modelling and advanced experiments to further deepen the understanding.

Section 2 is reviewing a variety of the researched and discovered cathode phases within the system which revealed

[a] Department of Materials Science and Engineering, The University of Texas at Dallas, Richardson, Texas 75080, USA.
[b] Hunt Energy Enterprises, LLC. Dallas, Texas 75201, USA
† Footnotes relating to the title and/or authors should appear here.
Electronic Supplementary Information (ESI) available: [details of any supplementary information available should be included here]. See DOI: 10.1039/x0xx00000x

the high complexity. This complexity highlights the need of characterization techniques including *in situ* and *operando* techniques, while acknowledging the traditional and accessible *ex situ* options. The electrochemical mechanisms on energy storage and materials degradation of literature are reviewed in Section 3, including important factors of the cathode material, pH, voltage window, and reversibility.[7,8] In the end, we provide our perspectives on the needs and directions towards a better understanding and optimization of Aqueous Zinc–Manganese-Oxide Batteries (AZMOBs).

2. Materials & Characterizations

Manganese oxides are known to have numerous polymorphs, especially under aqueous environment with dynamic interactions with proton, Zn ion, water molecular, polyanion, hydroxide, and hydrate-based compounds. Qualitative and quantitative characterization of these has been a contributor to the challenges in these studies, as reversible formation and dissolution are dynamic processes coupled to both pH and potential, which are found to vary during charge/discharge. This section has reviewed the researched and discovered materials under the umbrella of H-Zn-Mn-O-X systems, where X represents anions from electrolyte salts including sulphate, acetate, etc. To elucidate the complexity further, this section also introduces advanced *in situ* and *operando* characterization methods.

2.1 Mn-O phases

The value of manganese-based cathodes stems from desirable electrochemical capacity, natural abundance, low cost, and lesser toxicity, reflected in a long history of energy applications. Many manganese-based oxide material polymorphs arise from various arrangements of [MnO_6] octahedral units. Particularly, binary manganese dioxide (MnO_2) can broadly be classified into three structural categories, consisting of tunnel phase (*e.g.*, α-, β-, γ-, ε-, R- and T-MnO_2), the layered phase of δ-MnO_2 and the spinel phase of λ-MnO_2. These are displayed in Figure 1, with structures acquired from The Materials Project—compiled from high-throughput Density Functional Theory (DFT) calculations—and rendered in VESTA.[9,10] As favourable electrochemical capacity may follow from one- or two-electron manganese redox, as MnO_2's Mn^{4+} transitions to Mn^{3+} and Mn^{2+}.

Among the close-packed oxygen framework, the Mn–Mn distances across the dominant tunnel or interlayer structures are more commonly discussed in literature, derived from characteristic XRD peaks by Bragg's law and generally informing the practicality of Zn^{2+}, H_2O, and H^+ intercalation. As phase transformation/conversion and Mn^{2+} dissolution/deposition are evidenced as key mechanisms, many structures and stoichiometries related to MnO_2 are also introduced and outlined. Some crystal systems, space groups, and prevalent features are noted in the text and Table 1, while excellent mineralogical characterization by Post *et al.*[1] and electrochemical surveys of Chabre *et al.*[11] provide greater details into the structures themselves—many described in online mineralogical resources like mindat.org.

α-MnO_2 (hollandite) consists of 1 × 1 and the defining, larger 2 × 2 tunnels (7 Å), formed by edge-sharing double chains of [MnO_6] octahedra. Formation may be achieved hydrothermally with K^+ template ions—described as cryptomelane-like—and has been studied for Li^+ and Na^+ intercalation studies and so should be similarly well suited to Zn^{2+} insertion.[1,11–13] As such, hollandite has received perhaps the greatest attention among MnO_2 materials for the role of the cathode to Zn-ion batteries. Many researchers synthesize needle-like or rod-shaped α-MnO_2 crystals along [220] direction, resulting in tunnels up to a micron in depth.[3,14]

β-MnO_2 (pyrolusite) is rutile-like with a narrow 1 × 1 tunnel structure of 1D [MnO_6] chains among the oxygen hcp sublattice. The small tunnel size limits any additional ion insertion except by protonation. Fibre, or whisker, morphologies have similarly been synthesized and characterized by TEM micrographs and SAED by various methods.[14,15]

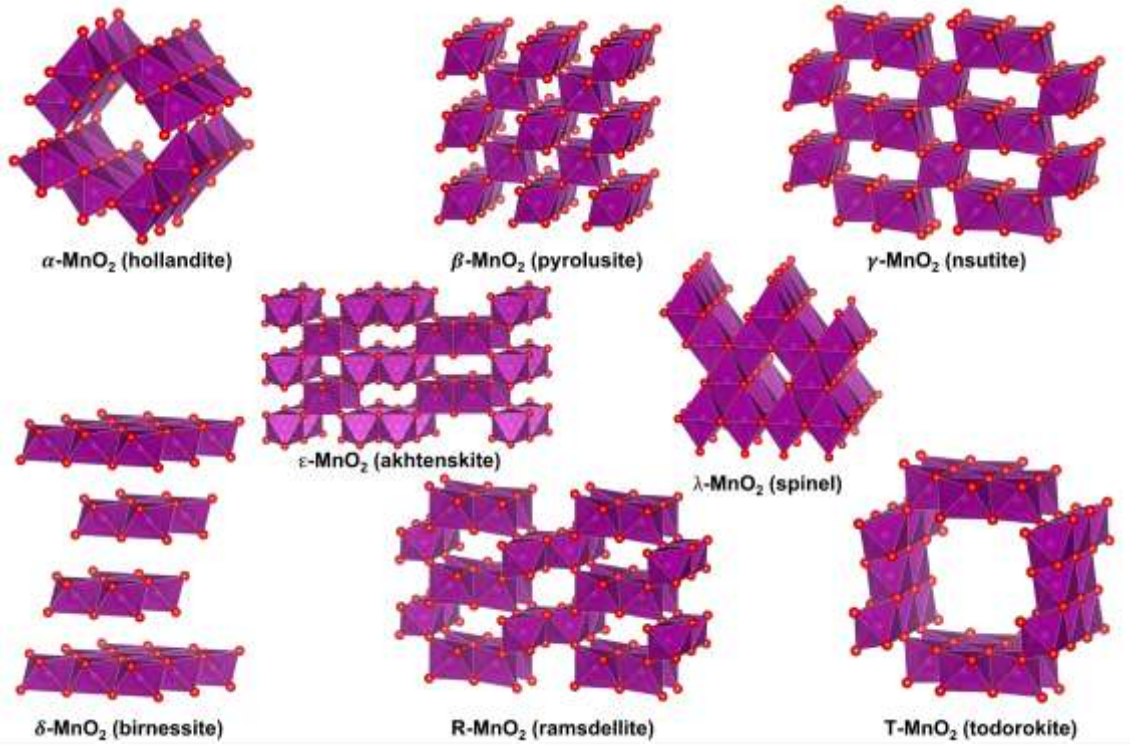

Figure 1 The various polymorphs of MnO_2 including hollandite (2 × 2 & 1 × 1 tunnels), pyrolusite (1 × 1 tunnel), nsutite (ordered 1 × 1 & 2 × 1 tunnels), akhtenskite (disordered 1 × 1 & 2 × 1 tunnels), ramsdellite (2 × 1 tunnel), todoroskite (3 × 3 tunnel), as well as layered birnessite and spinel phase. Manganese ions and octahedra are dark magenta, with red oxygen. Structures for each phase were acquired from www.materialsproject.org.[9] and rendered in VESTA.[10]

T-MnO_2 (todorokite) fundamentally displays tetragonal phase with $P_{4_2/m}$ space group, featuring an overly large 3 × 3 tunnel structure with relatively few studies of its application as a cathode in Zn-ion batteries.[16,17] Hydrothermal synthesis routes have utilized four-fold hydrated Mg^{2+} template ions to stabilize these large (~9 Å) tunnels.[12]

R-MnO_2 (ramsdellite) displays a regular 1 × 2 tunnel structure, with orthorhombic symmetry, P_{nma} space group (or P_{bnm} by swapping **a,b,c** to **c,a,b**).[12,18,19] The diaspore type structure, compared to the closely related rutile, yields two kinds of coordination for the oxygen atom, either planar with sp^2 hybridization or as the apex of a trigonal pyramid with sp^3 hybridization, which facilitates hydrogenation/protonation, and reduction of R-MnO_2 to groutite discussed below.[19,20] Intrinsic structural faults mean synthesis of ramsdellite often instead yields nsutite or akhtenskite, by relative degree of disorder.

***γ*-MnO_2 (nsutite)** has an intermixed structure of 1 × 2 tunnels of R-MnO_2 and 1 × 1 tunnels of β-MnO_2, by a limited number of faults and microtwinning—so-called "De Wolff disorder".[11,21] "Nsutite" may therefore sometimes refer broadly to a family of phases, or as a particular domain between ramsdellite and pyrolusite (rutile) with a smaller degree of De Wolff disorder. The moderately sized tunnels and two types of oxygens as in ramsdellite have led to a number of studies in *γ*-MnO_2 cathodes in various battery systems.[22] Such intrinsic disorder makes description of the nsutite family by atomic-scale simulations—such as DFT—limited or at risk of being disingenuous.

Mineral	Composition	JCPDS #	Mindat
Hollandite	*α*-MnO_2	42-1348	38–0476
Pyrolusite	β-MnO_2	24-0735	--
Nsutite	*γ*-MnO_2	24-0734	17-0510
Akhtenskite	*ε*-MnO_2	30–0820	--
Ramsdellite	R-MnO_2	07-222	--
Todorokite	T-MnO_2	18-1411	19-83
Birnessite	*δ*-MnO_2	80-1089	23-1046
Spinel	*λ*-MnO_2	44-0992	--
Manganite	*γ*-MnOOH	74-1842	18-805
Feitknechtite	β-MnOOH	74-1632	18-804
Groutite	α-MnOOH	74-1631 74-1049	24-713
Zn-birnessite	$Zn_xMn_2O_4{\cdot}nH_2O$	23-1046 19-1559	--
Zn-buserite	$Zn_xMn_2O_4{\cdot}nH_2O$	--	--
Vernadite	$Zn_xMn_2O_4{\cdot}nH_2O$	--	--
Zn-spinel (Hetaerolite)	$ZnMn_2O_4$	--	24-1133
Zn-spinel (hydrate)	$Zn_2Mn_4O_8{\cdot}H_2O$	09-0459[37]	--
Tunnel γ-Zn_xMnO_2	γ-Zn_xMnO_2	14-0644	--
Chalcophanite	$ZnMn_3O_7{\cdot}3H_2O$	--[36]	15-807
Woodruffite	$Zn_xMn_2O_4{\cdot}nH_2O$	47-1824	16-338

Table 1 Common names, designations, and some oft-cited JCPDF card no. of MnO_2 origin phases and products of Zn^{2+}, H^+, and H_2O intercalation- or conversion-based reactions in aqueous zinc-ion batteries with MnO_2 cathode.

Table 2 Reported performances of manganese oxides for mild-acidic aqueous Zinc ion battery

Phase	Electrolyte	Current collector	Voltage	Initial Capacity	Loading Mass	Cycling	Reference
α-MnO_2	2M $ZnSO_4$ + 0.2M $MnSO_4$	Self-supporting film	0.8-1.8 V	250 mAh/g	3-4 mg/cm^2	100 mAh/g after 300 cycles @ 0.1 A/g	6
β-MnO_2	2M $ZnSO_4$ + 0.5M nSO_4	Stainless steel foil	1.0-1.9 V	250 mAh/g	1 mg/cm^2	100 mAh/g after 1000 cycles @ 0.2 A/g	63
γ-MnO_2	1M $ZnSO_4$	Stainless steel mesh	1.0-1.8 V	250 mAh/g	N/A	150 mAh/g after 45 cycles @ 0.5 mA/cm2	22
δ-MnO_2	2M $ZnSO_4$ + 0.2M $MnSO_4$	Stainless steel foil	1.0-1.8 V	100 mAh/g	1.8 mg/cm^2	~25 mAh/g after 10000 cycles @ 5 A/g	29
ε-MnO_2	1M $ZnSO_4$ + 0.2M $MnSO_4$	Stainless steel mesh	0.8-1.9 V	300 mAh/g	3 mg/cm^2	~100 mAh/g after 500 cycles @ 3C	23
R-MnO_2	2M $ZnSO_4$	Carbon paper	1.1-1.9 V	150 mAh/g	2-4 mg/cm^2	~100 mAh/g after 1000 cycles @ 0.1A/g	19
T-MnO_2	1M $ZnSO_4$	Stainless steel foil	0.7-2.0 V	110 mAh/g	2 mg/cm^2	~90 mAh/g after 50 cycles	16
α-Mn_2O_3 /Mn_3O_4	2M $ZnSO_4$ + 0.5M $MnSO_4$	Stainless steel foil	0.8-1.9 V	392 mAh/g	1 mg/cm^2	140 mAh/g after 1000 cycles @ 1 A/g	32
MnO	2M $ZnSO_4$	Titanium foil	1.0-1.9 V	272 mAh/g	2 mg/cm^2	226 mAh/g after 100 cycles @ 0.1 A/g	33

ε-MnO_2 (akhtenskite) is ambiguously related to nsutite, pyrolusite, and ramsdellite featuring an irregular pattern of 1 × 2 and 1 × 1 tunnels, due to a high concentration of de Wolff disorder, many crystal micro-twinning defects and faults, and thus exhibit more diffuse diffraction lines.[11,21] Few AZMOB studies feature akhtenskite explicitly, due to the required care in distinction from nsutite, by both experimental and *ab initio* characterization.[23]

***δ*-MnO_2 (birnessite)** has a layered structure with a wide range of reported interlayer spacing, from a nominal van der Waals (vdW) gap ~4 Å and greater. The broader family as phyllomanganates in the basis of planar MnO_2 includes pristine δ-MnO_2 and its many forms altered by intercalates. Intercalation of ions and molecules may expand the vdW gap to, *e.g.* ~7 Å with the intercalation of Zn^{2+} and H_2O as hydrated birnessite.[24] Further hydration forms a double layer of water among intercalated ions, and distinguished as buserite, with 10~11 Å interlayer distance.[24,25] Hexagonal birnessite, over triclinic (*e.g.* Na-MnO_2), may exhibit Mn migration from planar to inter-layer octahedral sites, in some aqueous environments.[24,26,27] Morphological organization is sometimes reported as needle-like nanofibers, and some XRD and SAED patterns may suggest polycrystallinity, amorphous inclusions, or inhomogeneity as variants to pure δ-MnO_2 phase.[14,24,27] Accurate description of layered materials tend to require vdW-dispersion corrections to be explicitly accounted for. It is also reported that the MnO_2 layer spacing can be expanded through pre-intercalated ions like sodium or potassium, to facilitate the transport of Zn ions.[28,29]

***λ*-MnO_2 (spinel)** possesses a three-dimensional, metastable, spinel structure, with notably low porosity compared to many of its cousin structures. The relative cation deficiency compared to the full spinel structures, such as hausmannite, leave tetrahedral sites vacant, beneficiating diffusion pathways and may be satisfied occupationally as $ZnMn_2O_4$. High-quality λ-MnO_2 may be produced via Li^+ template ion and delithiation electrochemically or by acid leaching.[12] The larger Zn^{2+} ions are less suited to insertion than Li^+, thus making *λ*-MnO_2 subject to many doping and material engineering studies to improve electrochemical performance.[30]

Romanèchite MnO_2 is a monoclinic phase with 2 × 3 tunnels, achievable via two-fold hydrated Ba^{2+} templating. Very few studies involve synthesized romanèchite MnO_2 in the context of cathode to mild-acid electrolytes nor zinc-ion reaction products, though it is noted for its large tunnels, stabilized by intercalated barium and water.[12,31]

α-Mn_2O_3 has the dense cubic bixbyite structure, shown in Figure 2, and pure samples establish an orthorhombic crystal structure with $\mathbf{P_{bca}}$ space group.[32]

γ-Mn_2O_3 is hausmannite-like, (the spinel Mn_3O_4 structure, discussed below) with partial cation deficiency. Though less thermodynamically stable than α-Mn_2O_3 and Mn_3O_4, transient appearance during Mn^{2+} dissolution from Mn_3O_4 may occur.

ε-Mn_2O_3 uniquely exhibits the ilmenite ($FeTiO_3$) structure as a binary compound, with evenly divided Mn^{2+} and Mn^{4+}, mentioned for completeness, and as example of Mn^{3+} disproportionation.

Mn_3O_4 (hausmannite) as the spinel structure transformed to tetragonal $\mathbf{I_{4_1/amd}}$ space group relative to the cubic, cation-deficient λ-MnO_2. Among the close-packed oxygen sublattice as of λ-MnO_2, additional Mn^{2+} occupy tetrahedral sites, indicated as lighter magenta in Figure 2, while [$Mn^{3+}O_6$] octahedra show John-Teller distortions.[32]

MnO (manganosite) is as Halite, the common cubic rock-salt phase with $\mathbf{F_{m\bar{3}m}}$ space group. As a stable, though rarely occurring, mineral in nature, MnO is not typically synthesized for acidic battery materials, except favouring in more alkaline conditions—pH ~10-14 and potential < 0 V vs. SHE—as noted in the Pourbaix diagrams, Figure 3c. However, MnO can be a by-production of disproportionation reaction of Mn^{3+} → Mn^{2+} + Mn^{4+} due to the John-Teller distortions. Once the MnO comes into formation, Mn^{2+} can easily dissolve into aqueous solution which led to manganese dissolution. Due to dissolution of MnO,

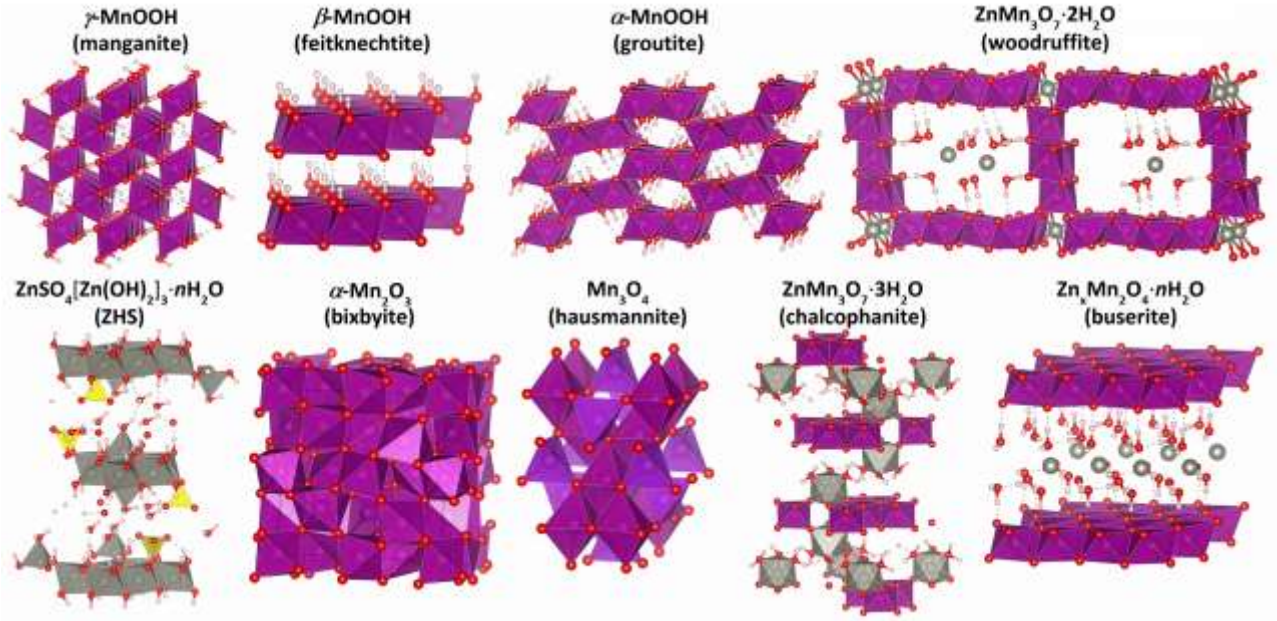

Figure 2 The three structures of mineral MnOOH polymorphs: manganite, feitknechtite, and groutite. Zn^{2+} and H_2O intercalated MnO_2 phases may form an expanded birnessite or buserite layered phases. Disrupted and reformed structures may adopt the 3 × 4 tunnel structure as woodruffite, or the broken layers of chalcophanite or woodruffite. Redistribution of manganese may yield Mn_2O_3, Mn_3O_4, or vernadite variant of the chalcophanite, while zinc salts form platelets of layered ZHS. Manganese ions and octahedra are dark magenta, with red oxygen, grey zinc ions and polyhedra, yellow [SO_4] tetrahedra, and small pink hydrogens. Structures rendered in VESTA.[10]

there has been report activating the MnO into MnO2 and demonstrating the performance.[33]

The majority of these manganese oxides phases have been demonstrated electrochemical activities by serving as pristine cathode materials. The example oxides and their battery performances have been summarized in Table 2. Due to the complexity and debates of this system in fundamental electrochemical mechanism (discussed in more details in Section 3), the differences in loading mass, current density, electrolyte composition and voltage range will have determining impacts on the stability interpretation; it is therefore hard to draw the conclusion regarding which one is better or worse. It is one of our perspectives to have more practical conditions in order to evaluate this system and will be detailed in Section 4.

2.2. H-Mn-O phases

With a mild-acidic aqueous electrolyte interface, the cathode inevitably interacts and/or reacts with the present ions. As will be discussed later, pH and voltage windows largely dictate the behaviour, where hydroxide and hydrated manganese-oxide phases have been reported. The weakly-bound species—protons or water molecules—introduce challenges to conventional characterization method, but mineralogists have often characterized related materials through synchrotron X-ray or neutron diffraction techniques.[1,19,27]

H^+/MnO_2 reactions yield structures with some intrinsic complexities. Chabre and Pannetier[11] summarized challenges in discussing some of the above MnO_2 given the nature of structural defects. Further, they discuss the protonation of MnO_2 phases and the characterization of the most common resulting MnOOH phases. Numerous studies of protonation of MnO_2 and in alkaline environments evolved understanding of electrochemical behaviour from late 1950s through early 2000s, and often adopted a shorthand keyed to suggesting Mn reduction, *i.e.* MnOOH as $MnO_{1.5}$. The competition between H^+ and Zn^{2+} in reaction mechanisms will be discussed in Section 3, and characterization techniques to contrast these cases will be discussed in Section 2.5. Prominently, structural characterization can capture the significant deformation due to Jahn-Teller distortion of Mn^{3+} while implementation of advanced techniques is encouraged for accurate distinction between increased structural defects, Zn^{2+} intercalation, and protonation (H^+ intercalation).

MnOOH has three natural polymorphs and more derived by reduction of a respective MnO_2 phase. Each bears similarities to a given MnO_2 host phase, with replacement of half of the oxygens with hydroxyl anions and distortion of the Mn(III) octahedra by Jahn-Teller effects.[1] **Manganite (γ-MnOOH)** crystal structure is shown in Figure 2a, similar to pyrolusite β-MnO_2 in terms of 1 × 1 tunnel structure and affinity for whisker morphology. **Groutite (α-MnOOH)** is isostructural with ramsdellite (R-MnO_2, orthorhombic), with distortion displayed in Figure 2. The layered **feitknechtite (β-MnOOH)**, appears as protonation of every other oxygen of the layered birnessite phase, *δ*-MnO_2, but has conversely been considered as the partial oxidation product of $Mn(OH)_2$. Lastly is unnamed **δ-MnOOH** which, like γ-MnO_2, is described with random intergrowth of groutite and manganite layers with De Wolff disorder, thus leading to broader XRD lines than groutite.

$Mn(OH)_2$, or pyrochroite, follows from full reduction by protonation of layered *δ*-MnO_2 and/or β-MnOOH with every oxygen protonated as hydroxyls. These form edge-sharing planes of Mn-OH octahedra, held together by hydrogen bonding. Mineral

pyrochroite would follow space group $P_{\bar{3}m1}$, isostructural with $Cd(OH)_2$.

2.3 Zn-Mn-O phases

Most typically reported products of Zn-MnO_2 charge/discharge are presented by common name, phase designation, and JCPDS no. in Table 1. Key features and relations of these phases are given in brief in the following.

Zn-birnessite, may be distinguished as (Layered) L-Zn_yMnO_2, intercalating Zn within δ-MnO_2 interlayer spaces.[34] The electrostatic interactions between the Zn^{2+} and planar oxygens shrink the interlayer distance, thus shifting the lowest angle (001) 2θ diffraction angle. In the aqueous environment under bias, intercalation of both Zn^{2+} and H_2O instead increases interlayer spacing, to ~7 Å, much like the tunnel size of α-MnO_2. Intercalated H_2O may also lower the barrier to planar gliding, inducing disorder to the birnessite stacking order, potentially leading to a layered **vernadite**-type $Zn_xMnO_2{\cdot}nH_2O$ (chalcophanite) or $Zn_xMnO(OH)_y$[35,36] as illustrated in Figure 2.

Zn-buserite follows from sufficiently hydrated Zn-birnessite, with double water layers surrounding intercalated zinc-ions.[25] The interlayer distance is identified to be around 11 Å, comparable to structure dimensions of Todorokite-MnO_2 and woodruffite tunnels, which feature triple chains of edge sharing [MnO_6] octahedra. Many instances of Zn-birnessite as reaction products in *ex situ* XRD characterization are suspected to be made in error, as an indirect product of dried buserite, which is more commonly reported by *in situ* and *operando* characterization.

Spinel $ZnMn_2O_4$ or hetaerolite can form by intercalation of Zn into various MnO_2 phases, occupying tetrahedral sites of the previously discussed λ-MnO_2 structure, and is isostructural with hausmannite.[37] Many studies report formation may follow distortion or conversion processes. The rise of Jahn-Teller distorted Mn^{3+} (high spin $3d^4$, $t_{2g}^3e_g^1$) during Zn^{2+} intercalation has been indicated as a source of electrode degradation by rapid capacity loss, though others also note near 100% coulombic efficiency, indicating such transformation is not irreversible.[38]

Chalcophanite $ZnMn_3O_7{\cdot}3H_2O$ ($Zn^{2+}Mn^{4+}{}_3O_7{\cdot}3H_2O$, Figure 2) with trigonal crystalline symmetry, consisting of incomplete MnO_2 layers, spaced at about 7 Å.[39–41] In the interlayer space, divalent ions, particularly Zn^{2+}, are octahedrally coordinated with H_2O molecules and basal plane oxygens—the corner-

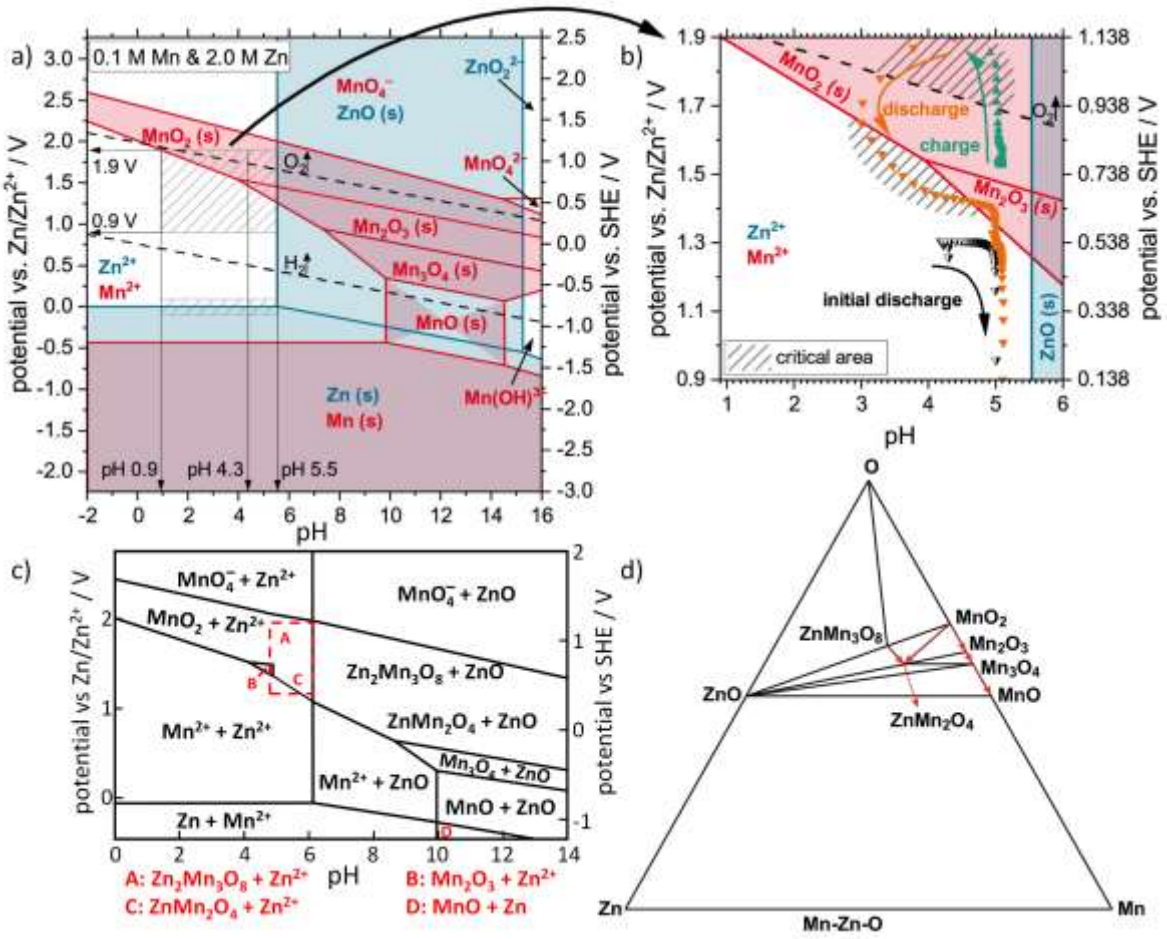

Figure 3 a) overlaid Pourbaix diagrams for Zn and Mn in aqueous solution, with working window voltage shifted from SHE (right) to Zn/Zn2+ anode (left), and b) focused on mild and weak acidic pH range, including plotted charge/discharge pathways. Reproduced with permission,[43] thermodynamic data provided by Materials Project of the University of California at Berkeley, www.materialsproject.org.[10] Copyright 2020 Journal of The Electrochemical Society. c) Pourbaix diagram including thermodynamic Zn-Mn oxide reaction products and d) corresponding Zn-Mn-O phase diagram. Reproduction with adjustments for clarity, under the Creative Commons license http://creativecommons.org/licenses/by/4.0/[2]

Table 3 Zinc oxide and sulfate compounds, including various ZnLDH (ZHS) related phases that may be present in aqueous zinc-ion batteries.

Compound	JC-PDS no.
ZnO	01-089-7102
Zinc oxy-sulfates	031-1469, 071-2475, 016-0821
$Zn_5O_2(SO_4)_3$	00-016-0305
$ZnSO_4[Zn(OH)_2]_3$	00-044-0675
$ZnSO_4[Zn(OH)_2]_3{\cdot}0.5H_2O$	00-044-0674
$ZnSO_4[Zn(OH)_2]_3{\cdot}4H_2O$	00-044-0673
$ZnSO_4[Zn(OH)_2]_3{\cdot}5H_2O$ (Osakaite)	04-012-8289 00-060-0655
$ZnCoNi(OH)_2SO_4{\cdot}5H_2O$	00-046-1276

sharing oxygen of the MnO_2 layer's vacancy sites—as shown in a hexagonal-like construction displayed in Figure 2.[36,39–41]

Aurorite ($Mn^{2+}Mn^{4+}{}_3O_7 \cdot 3H_2O$) also falls within the chalcophanite group, with the same layered structure, but Mn^{2+} rather than Zn^{2+} in the interlayer. Consequently, the diffraction patterns (e.g., aurorite: ICDD 19-88; chalcophanite: ICDD 15-807) are nearly indistinguishable.

Woodruffite, commonly $ZnMn_3O_7{\cdot}2H_2O$, though with general formula $Zn^{2+}{}_{x/2}(Mn^{4+}{}_{1-x}Mn^{3+}{}_x)O_2{\cdot}nH_2O$, displays a monoclinic structure.[42] The $ZnMn_3O_7{\cdot}2H_2O$ stoichiometry contains 3 × 4 tunnels with Zn^{2+} occupying the tunnel walls intersections and partially solvated within the large tunnels, as in the example rendered in Figure 2. Like chalcophanite, formation is expected to arise from some original tunnel or layered MnO_2 through intercalation of both Zn ions and water molecules. The irreversibility of woodruffite formation, or kinetically prohibited transformation back to MnO_2, is discussed with respect to degrading capacity in Section 3.3.

The thermodynamic stability of solid and solvated phases within Zn-Mn-O system in aqueous environments can be compiled into Pourbaix diagrams (E_H–pH or pE/pH diagrams), as shown in Figure 3a-c.[2,43] During charge/discharge, bounds set by oxygen evolution reactions (OER) and hydrogen evolution reactions (HER) define the working voltage window at given pH, shown by the dashed lines in Figure 3a, with reference anode potential adjustment from SHE (right axis) to Zn/Zn^+ (left axis), as the relevant counter-electrode for discussed Zn-MnO_2 batteries. Considering mild acidic (pH 6~4) electrolytes of interest set the final bounds of many studies, with example in Figure 3b displaying the coupling of pH and voltage. However, H^+ and H_2O intercalated species are absent from Pourbaix diagrams. Hydrated phases precipitated from solution have been widely reported in recent literature as will be explored in the following section.

2.4 H-Zn-Mn-O-X phases

With proton involvement in the activity, the dissociation of water molecular within the electrolyte leads to the generation of extra OH^- as well. When OH^- binds with electrolyte Zinc salt, such as ZnSO4, zinc hydroxide sulfate pentahydrate (ZHS) may then form. ZHS and related compounds form a layered structure consisting of stacked $Zn(OH)_2$ sheets with water molecules and anionic compounds in the interlayer spaces. Given the proclivity of $ZnSO_4$ salts chosen as Zn^{2+} source in aqueous electrolyte, the by-product is most commonly ZHS, with a general formula of $xZn(OH)_2{\cdot}yZnSO_4{\cdot}zH_2O$ for variable values *x, y*, and *z*, and typical stoichiometry of $ZnSO_4[Zn(OH)_2]_3{\cdot}zH_2O$ with z = 1/2, 1, 3, 4, or 5—the most commonly reported.[44,45] Ambiguously, these may be referred to as Zinc Sulfate Hydroxide Hydrate (ZSH), Zinc Hydroxide Sulfate (ZHS), Basic Zinc Sulfate (BZS), Zinc Basic Sulfate (ZBS), or Zinc-layered double hydroxide (ZnLDH), with an assumed but unstated H_2O content. Scanning electron microscopy (SEM) commonly identifies ZHS by morphology—forming hexagonal platelets—and by EDS, with high concentration of Zn and presence of sulphur.[44,45]

Comparative study of 1 M zinc sulfate [$ZnSO_4$, pH≈4] to alternative Zn-salts including 1 M zinc acetate [$Zn(CH3COO)_2$, pH≈6] and 1 M zinc triflate [$Zn(CF_3SO_3)_2$, pH≈4], yielded ZHS analogues: zinc hydroxyacetate [$Zn_5(OH)_8(CH_3COO)_2{\cdot}nH_2O$](ZHA)[46–48] and zinc hydroxytrifalte [$Zn_5(OH)_8(CF_3SO_3)_2{\cdot}nH_2O$] (ZHT),[46,48,49] respectively. The formation of ZHS is closely associated with pH level changes of electrolyte and comparable reversibility.

Due to varying hydration states, the most intense characteristic X-ray diffraction (XRD) peaks of ZHS are spread over a wide range of Bragg angles. Further, a manganese-zinc compound, $Mn_xZn_y(OH)_zSO_4{\cdot}5H_2O$, is a ZHS analogue structure recently reported by Stoševski *et al*.[37] as Mn-Zn-layered double hydroxide (MnZnLDH), identified by subtle differences between the common Osakaite (ZHS-pentahydrate) and Guarinoite, $ZnCoNi(OH)_3SO_4{\cdot}5H_2O$. They postulate its presence has been erroneously misidentified as ZHS in much of the literature, due to largely similar XRD patterns. As well, they indicate Mn concentration and high pH gives co-precipitate spinel and hydrated spinel: $ZnMn_2O_4$ and $Zn_2Mn_4O_8{\cdot}H_2O$, noted in Table 1. There have been controversies on whether ZHS-like compounds play an active or passive role in AZMOBs with MnO2 cathodes, and whether it is involved with redox reactions. The topic will be explored in more details in Section 3.

2.5 Characterization Methods

Given the high complexity of phases existing in the AZMOBs, and the dynamic processes and myriad—potentially metastable or transient—species to identify, appropriate characterization entails at least one of X-ray diffraction, scanning electron microscopy, transmission electron microscopy (often implementing selected-area electron diffraction, electron energy-loss spectroscopy, and energy dispersive spectroscopy), Raman or infrared spectroscopy, or X-ray absorption spectroscopy related techniques—often two or three—with respective abbreviations outlined in Table 4. Recent contrast of *in situ* characterization to—the more readily available—*ex situ* studies have found notable differences that have likely contributed to misinterpretations and conclusions based on earlier *ex situ* characterization. *In situ* and *operando* techniques as shown in Figure 4, provide great benefits of capturing dynamic processes, that may include complex, multi-step phase evolution during discharge/charge.[50,51] *In situ* and *operando* techniques bear a greater barrier to entry, however, such as a

synchrotron X-ray source, beam time, and appropriately modified coin cell geometry—or jelly roll/pouch cell.

A wide variety of complementary material and electrochemical characterization techniques are summarized in Table 4. X-ray characterization and Cyclic Voltammetry are each essential in discussing material preparation, cycling performance, electrochemical activities, and reaction product identification. Reporting initial phase cathode material via XRD is standard practice in conjunction with synthesis methods, while **SEM** and/or **TEM** micrographs provide useful supplemental details, such as nanocrystallinity and morphology for engineered microstructures—nanorods, needles, platelets, or nano-flowers. Powder XRD (**PXRD**) provides broad, bulk characterization, while high resolution TEM (**HR-TEM**) and **SAED** patterns may provide local crystal phases and are most typically available *ex situ*. Most significantly, **XRD** and **TEM-SAED** diffraction patterns provide convenient phase identification, matching relative intensities of characteristic peaks to distinguish and de-convolute contributing phases. Limitations arise, however, in instances where several present phases may share similar and/or shifting characteristic peaks due to variable water content, as with Zn-buserite (as fully hydrated Zn-birnessite) and ZHS structures, that may also align with Todorokite-MnO_2. As mentioned above and to be described in more detail concerning the evolving mechanistic understanding, *ex situ* characterizations of cycled cathode materials are being approached with greater scepticism. Through standard practices in sample preparation, reaction products present during cycling may have inadvertently been altered through washing/drying processes and important details obfuscated to early researchers.

In turn, the importance of elemental composition and distribution is increasingly highlighted in the face of conflicting electrochemical mechanisms. Intercalation of Zn^{2+} into cathode material structures versus the formation of ZHS-type phases provide alternate roles and end products. Finding consensus regarding the competing mechanisms (Section 3) will rely on comprehensive analysis, to distinguish potential intercalates, converted phase, and dissolution/deposition reaction products. Most characterization techniques, however, are insensitive to the presence and location of hydrogen, necessitating niche techniques like Nuclear Magnetic Resonance (**NMR**), **neutron diffraction**,[27] or indirect detection, *e.g.,* by inferring the role and concentrations of H^+ from structural transformations or chemical shifts in the presence/absence of Zn^{2+}. Vibrational spectroscopy techniques—Fourier transform infrared spectroscopy (**FTIR**) and **Raman** spectroscopy—are also available *ex situ* (or by specialized *in situ* experimental

Table 4 Typical techniques implemented to characterize battery materials and electrochemical performance.

Technique	Abbreviation	Condition	Quality
X-ray Diffraction (XRD)	XRD	*In situ/ ex situ*	Bulk crystalline phase
Synchrotron/High-Resolution X-ray Diffraction	HR-XRD	*In situ/ Operando*	Bulk crystalline phase
X-ray Absorption Spectroscopy (XAS)	XAS	*Operando*	Composition
Soft XAS-ray Absorption Spectroscopy	sXAS		Elemental Charge State
X-ray Absorption Near Edge Structure	XANES		Elemental Charge State
Extended X-ray Absorption Fine Structure	EXAFS		Bond Lengths
X-ray Photoelectron Spectroscopy	XPS	*Ex situ/ Operando*	Elemental Charge State
X-ray Fluorescence Spectroscopy	XRF	*Ex situ/ Operando*	Elemental Composition
Scanning Electron Microscopy	SEM	*Ex situ*	Morphology
Energy Dispersive (X-ray) Spectroscopy	EDS/EDX/XEDS	*Ex situ*	Elemental Mapping
Transmission Electron Microscopy (Environmental)	TEM	*Ex situ/ (Operando)*	Microstructure
Selected-Area Electron Diffraction	SAED		Micro-crystalline phase
Electron Energy Loss Spectroscopy	EELS		Elemental Mapping
Energy Dispersive (X-ray) Spectroscopy	EDS/EDX/XEDS		Elemental Mapping
Raman Spectroscopy	Raman	*In situ/ Ex situ*	Bond Structure
Fourier Transform Infrared Spectroscopy	FTIR	*In situ/ Ex situ*	Bond Structure
Inductively Coupled Plasma Optical Emission Spectrometry	ICP-OES	*Ex situ*	Elemental Composition
Nuclear Magnetic Resonance Mass Spectrometry	NMR-MS	*In situ*	Proton Distribution
Thermal Gravimetric Analysis	TGA	*Ex situ*	H_2O content and thermal stability
Cyclic Voltammetry	CV	--	Capacity, Specific Capacity, Coulombic Efficiency
Electrochemical Impedance Spectroscopy	EIS	--	Conductivity
Galvanostatic Intermittent Titration Technique	GITT	--	Open-Circuit Voltage (OCV)
pH microelectrode	--	*Operando*	pH

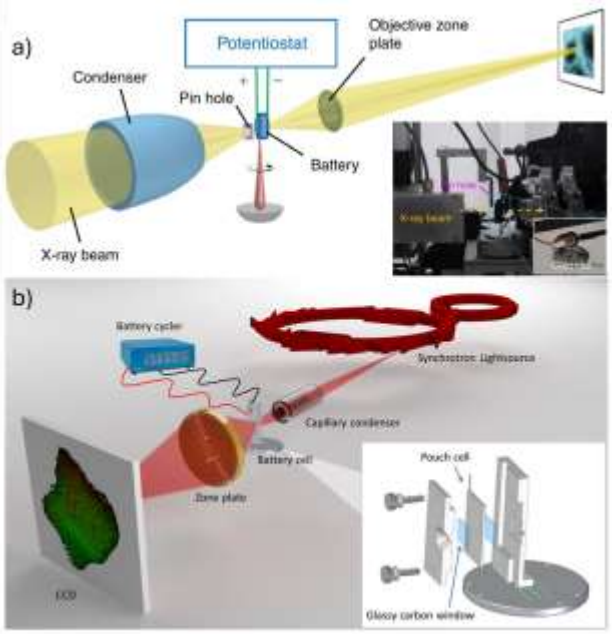

Figure 4 (a) The principle of full-field transmission X-ray microscopy at X8C beamline, National Synchrotron Light Source. The lower right insert shows a photo image of in *operando* electrochemical measurement at X8C. Courtesy of Brookhaven National Laboratory. Reproduced with permission.[50] Copyright 2014 Springer Nature; (b) Schematic drawing of the setup used for *in situ* spectro-microscopic study of LIBs (not to scale). The lower right inset shows a detailed view of the developed battery pouch cell system that allowed the *in situ* study of $LiCoO_2$ particle's long-term cycling behaviour. Reproduced with permission.[51] Copyright 2017 American Chemical Society.

apparatus) to distinguish relevant phases.[26,52] Besides protonation, separate complications arise from intercalated H_2O molecules commonplace in the large-tunnel or layered materials; thermal gravimetric analysis (**TGA**) can provide useful information about hydration (H_2O content).

Elemental mapping is most conveniently conducted by SEM-, TEM-, or **STEM-EDS** (scanning transmission electron microscopy)-(energy dispersive spectroscopy), for surface and bulk composition by cross-section TEM, respectively. Material samples collected from test cell batteries at various states of charge/discharge are commonly reported on, analysing phase, microstructure, morphology, and elemental mapping to identify reaction products throughout electrochemical processes. In the absence of (rare) environmental TEM experiment setups, however, sample preparation techniques may yet again obfuscate direct reaction products.

Compelling data arises, then, from *operando* X-ray characterization, as implemented with synchrotron X-ray sources. Capabilities include much greater penetration depth, time-resolved,[36] and high-resolution X-ray diffraction (**HR-XRD**) variants granted by synchrotron hard X-ray sources (energy > 10,000 eV), to non-diffractometry-based characterization: X-ray absorption spectroscopy (**XAS**) techniques such as X-ray absorption near-edge spectroscopy (**XANES**) or extended X-ray absorption fine-structures (**EXAFS**). These may be applied to give valuable insights into elemental charge states and bond lengths, as well as characterizing bulk properties of poor or non-crystalline materials.[26,48] Similarly, *operando* X-ray photoelectron spectroscopy (**XPS**) has been reported in many cases, inferring Mn redox activity by shifts to valence electron binding energy.[53] Additionally, X-ray fluorescence spectroscopy (**XRF**) can offer elemental composition details, including micron-scale spatial resolution by μ-XRF, though without information regarding oxidation state.[5] The cost (and availability of beam time), specially prepared coin-cells, and requisite expertise to acquire *operando* XAS, or XPS data, however, is often prohibitive to the median research group, and so, bridging *in situ*/*operando* with *ex situ* characterization to ensure compatibility in cross-referencing and future research endeavours is of interest to all participants.

For all studies of battery materials, electrochemical characterization generally entails a minimum of **cyclic voltammetry**, reporting voltage-capacity (**CV**) curves and charge/discharge profiles. Key parameters, such as charge rates, cut-off voltages, and active material mass are essential to report, and as further studies attempt to report improvements to capacity—e.g. by structural engineering—areal capacity and degradation trends are valuable to report at practical charge rates for meaningful comparisons. Supplemental electrochemical characterizations include electrochemical impedance spectroscopy (**EIS**) and galvanostatic intermittent titration technique (**GITT**), which are implemented to derive diffusion coefficients, rates, and conductivity, but require informed experimental design, including knowledge of present phases, for meaningful data interpretation.

As will be discussed below, additional measurement techniques to observe changes to local pH and solvated cation concentrations—Mn^{2+} and Zn^{2+}—have provided great insights. Titration with a standard reagent may traditionally provide a measure of pH , but greater quantification by pH microelectrode has permitted measurement of local pH changes correlated with certain phase formation, and cross reference with Pourbaix diagrams for insights regarding reactions as in Figure 3b.[43] Associated changes to solvated Mn^{2+} and Zn^{2+} concentration are measurable by spectroscopy techniques such as electron paramagnetic resonance spectroscopy (**EPR;** also called electron spin resonance spectroscopy, ESR), atomic absorption spectroscopy (**AAS**) or optical emission spectroscopy (**OES**)—as with the characterization of solid phase, these provide the greatest insights if they can be conducted *in situ*/*operando*.[54,55] Related, inductively coupled plasma (ICP) spectroscopy techniques may provide quantitative measurements of elemental composition, to varying sensitivities and detection limits. Inductively coupled plasma mass spectroscopy (ICP-MS) may be sensitive to concentrations on the order of parts-per-trillion (ppt) but requires complete and dilute dissolution of solid species with stricter tolerances (~0.2%), whereas **ICP-OES** may detect ppb and at much more lax tolerance (up to ~30%).

Whether *ex situ* or *operando*, the above techniques often rely on previous works for accurate characterization. Much the foundational study of MnO_x span decades of literature on a rich variety of mineral phases, alkaline batteries, and recent refinements in light of present studies, tracing back to Chabre, Moezzi, Post, Wadsley, *et al.*.[1,11,17,19,24,26,27,31,36,39–42,52,53,56]

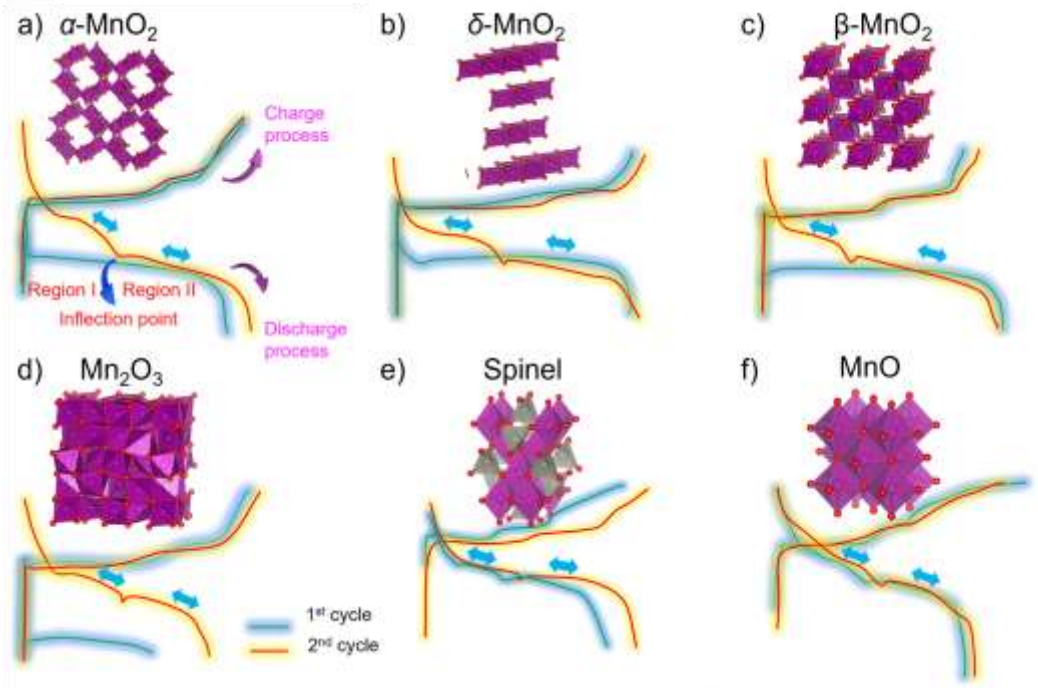

Figure 5 The representative charge-discharge curves show consistencies across different phases of MnO_x cathodes to aqueous zinc batteries. The two regions, persistent in these systems, should be considered in discussion of mechanisms including (de)intercalation, conversion, and dissolution/deposition methods reactions. Reproduced with permission.[7] Copyright 2022 Elsevier Inc. Structures re-rendered in VESTA.[10]

3. Electrochemical Mechanisms

3.1 Storage Mechanisms

In the interest of achieving long cycle-life and high capacity, comparisons of performance are often a feature of reports. A critical review of the literature base by Nazar *et al.*,[57] however, has reasonably stressed the importance of reporting characterization at practical charge rates. The stark contrast in capacity and degradation at high-rate versus low-rate cycling performance is telling of the hidden complexities to the electrochemical mechanisms that challenge the applicability—or at least versatility—of rechargeable AZMOBs.[58] Among the many reviews of late, there are many recounts and categorizations of the reaction mechanisms suggesting approximately six mechanisms, for various MnO_2 cathode materials.[7,14] An analysis of such cathode materials by Sambandam *et al.*[7] highlighted the two-plateau feature generally present in many MnO_x compounds, as in the reproduced Figure 5. As the most extensively studied MnO_2 cathode material, α-MnO_2 has been presented to exhibit each of these six potential reaction mechanisms: **Zn^{2+} intercalation**,[13,22,34,59,60] **H^+ intercalation**,[3,6,61] **H^+ and Zn^{2+} co-intercalation**,[2,29,62] and more intricate mechanisms including **chemical conversion reaction induced by H^+ and/or Zn^{2+} intercalation**,[2,3,58,63] **Mn^{2+} dissolution-deposition**,[5,54,55,64] and **ZHS driven reactions**.[44,65,66]

In the following sections, we will first discuss the intercalation-based, then more complex reactions. Follow-up discussion regarding degradation mechanisms, noting the progression of understanding the system, driving each new mechanism proposed.

3.1.1 Zn^{2+} intercalation/de-intercalation is much the same as the conventional intercalation mechanism of rechargeable Li-ion batteries, often layered metal-oxides. For application as cathode in rechargeable battery, the many polymorphs of MnO_2 that feature one-dimensional tunnel (α-, β-, γ-, and *R*-MnO_2), two-dimensional planar (δ–MnO_2), and three-dimensional (λ-MnO_2, spinel) structures are conceptually well suited to highly-reversible ion intercalation—or "insertion"—chemistry. Intercalation of Zn^{2+} ions is the most intuitive electrochemical mechanism, much as Li^+ intercalation in Li-ion batteries. Thus, this was assumed in the preliminary resurgence of studies *ca*. 2012, by Xu *et al.*,[13] accepted for many years. As the most fundamental and straight-forward, intercalation of Zn^{2+} into an MnO_2 cathode—as the sole electrochemical mechanism—is discussed as **Mechanism 1**. Such a reversible reaction formula would during discharge/charge would look like Eq. 1.

$$\boldsymbol{MnO_2 + xZn^{2+} + 2xe^- \leftrightarrow Zn_xMnO_2} \quad (1)$$

3.1.2 H^+ intercalation/de-intercalation gained prominence in study upon a report by Pan *et al.*[3] in 2016 asserting H^+ intercalation—rather than Zn^{2+}—is the exclusive electrochemical mechanism and is designated **Mechanism 2**. As introduced in Section 2, the mildly acidic aqueous electrolytes—adopted for rechargeable AZMOBs—present proton concentrations liable to induce H^+/MnO_x reactions. Mechanism 2 was credited by the prevalence of MnOOH reported by *ex situ* XRD characterization, demoting the role of Zn^{2+} to ZHS formation as a by-product, kinetically inhibited from intercalation with corroboration by symmetric Zn|Zn cells, alternate cathodes, and later *in situ* studies.[3,61]

Consideration of these reactions' reversibility has evolved in subsequent studies, with further discussion with respect to other mechanisms to follow. Eq. 2 presents the general and

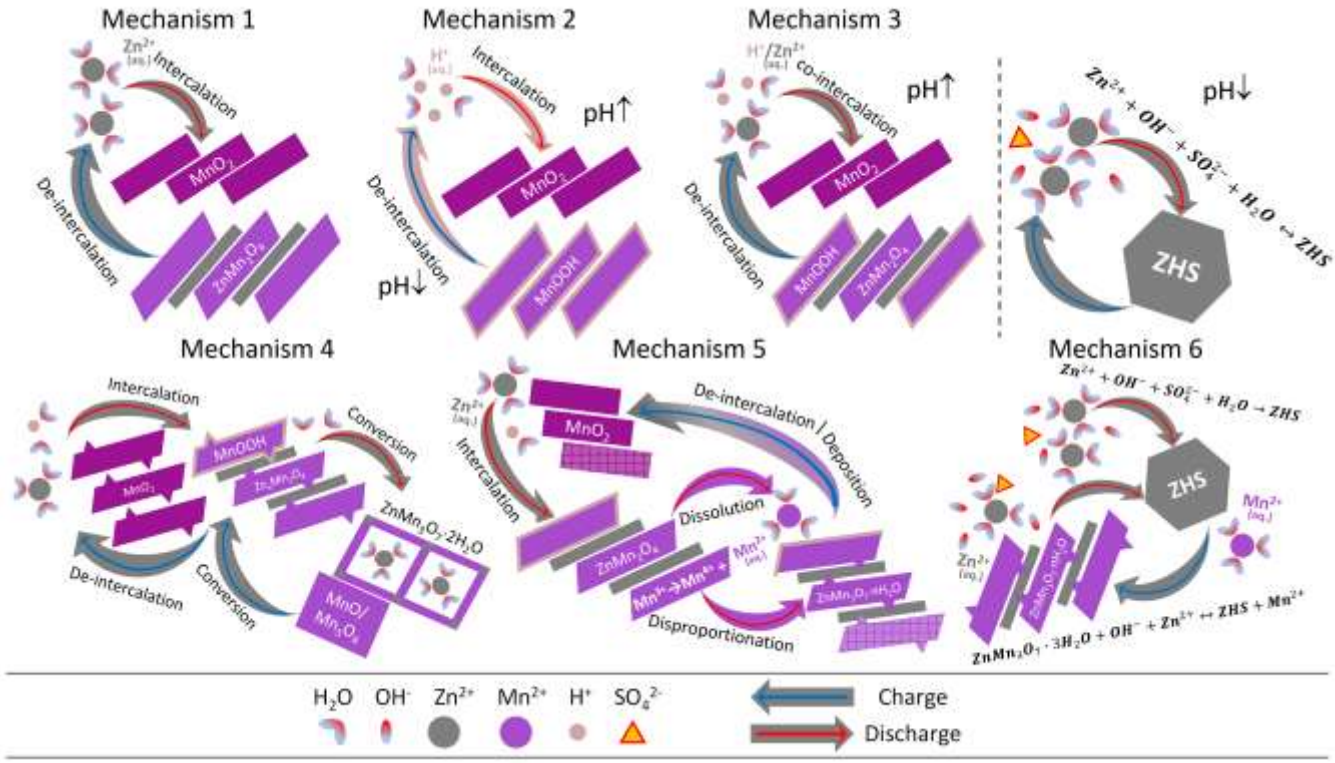

Figure 6 Cartoon diagrams illustrating reaction mechanisms, ranging from simple intercalation/de-intercalation to significant conversion mechanisms and complex sequences. Mechanisms 2, 3, and 4 intrinsically change pH, to be balanced by reversible formation of ZHS platelets as byproduct consuming OH^-, while Mechanism 6 includes ZHS/chalcophanite transformation as direct contribution to capacity. Discharge reactions progress as directed by inset red arrows and charge cycle reactions by inset blue arrows.

accepted H^+ intercalation reaction at 1.2 V discharge, with ambiguous MnO_2 and MnOOH microstructure:

$$\boldsymbol{MnO_2 + H^+ + e^- \rightarrow MnOOH} \quad (2)$$

As Eq. 2 proceeds with discharge (and reverses during charge), H^+ concentration, $[H^+]$, in the electrolyte decreases (increases), with corresponding increase (decrease) of pH, particularly local to the cathode. Consequences including change in proton activity and ZHS formation—considered then as a by-product to balance $[OH^-]$—will be discussed in more detail in the following sections.

3.1.3 Zn^{2+}/H^+ co-intercalation/de-intercalation as the combination of the previous two was—logically—the next assertion made in 2017 by Sun *et al.*,[62] presented as **Mechanism 3**. Distinct plateaus in CV profiles, distinguished as Region I and Region II in Figure 5—as well as two distinct redox peaks in galvanostatic studies—are interpreted as two subsequent reactions. EIS, GITT, and *ex situ* XRD indicated subsequent and kinetically distinct reactions at different depths of discharge.[2,3,62,67] Small and mobile H^+ are considered kinetically favoured for diffusion within the cathode structure, and so are intuitively assigned to Region I, while the slow diffusion of bulky and higher-charged Zn^{2+} then correspond to Region II.

Supporting the progression in diagnosing these mechanisms, electrochemical study of MnO_2 in the absence of Zn^{2+} ions—by cycling in a 0.2 M $MnSO_4/H_2O$ electrolyte—exhibited a single voltage plateau between 1.8 V and 1.35 V, attributed to H^+ intercalation. Similarly, an electrolyte absent of H^+, such as $ZnSO_4$/dimethyl sulphoxide (DMSO)—reported by Zhao *et al.*[68]—produced a single, separate plateau as well, thereby lending credence to the co-intercalation/de-intercalation mechanism. Zhao ceded that the added aqueous Mn^{2+} may also play a role—a mechanism to soon gain attention.[68] Nevertheless, many studies have since included both $ZnSO_4$ and smaller concentrations of $MnSO_4$ and capture two distinct voltage plateaus in charge/discharge profiles, as Region I and Region II, as in Figure 5, corresponding to fast H^+ insertion followed by kinetically slower Zn^{2+} intercalation, respectively.

Here, too, pH change and ZHS formation had been neglected or considered benign. Poor cyclability and failure to mitigate degradation was telling that further studies were essential, leading to the following mechanisms and discussion.

3.1.4 Intercalation and conversion as a mechanism originates from inherent instabilities of Mn^{3+}. Intercalation of ions into MnO_2 cathodes during discharge—regardless of completeness as a mechanism—bears consequences one must consider for MnO_2 cathode stability. In an example of Zn^{2+} intercalation—whether into the tunnels, layers, or spinel tetrahedral sites—full theoretical discharge terminates at x = 0.5 in Eq. 1, yielding the stoichiometry of $\boldsymbol{Zn^{2+}Mn_2^{3+}O_4^{2-}}$, highlighting the nominal charge state of the manganese cation.[2] Similarly, and already introduced in Section 2.2, $\boldsymbol{Mn^{3+}OOH}$ follows from Eq. 2, similarly inducing Mn^{3+}—the crux of MnO_2 cathode stability.[3] Reduction of Mn^{4+} to Mn^{3+} upon ion intercalation results in $3d^4$ electronic state occupation, better expressed as high-spin $\boldsymbol{t_{2g}^3 e_g^1}$ of the MnO_6 octahedral crystal field representation.[69,70] The e_g state occupation induces significant Jahn-Teller effects and drives geometric distortion by two elongated bonds relative to

four co-planar bonds (+Q_3).[69,70] The related instability pushes the system toward disproportionation: $2Mn^{3+} \rightarrow Mn^{2+} + Mn^{4+}$. This begets further structural reordering, due to mismatched ionic radii, or Mn^{2+} dissolution with appropriate evolution of stoichiometry near the surface. The following discussion consider the consequences of this redox activity, including conversion, dissolution, and deposition reactions as components of the following mechanisms.

The intercalation/conversion dual mechanism was put forward explicitly by Li *et al.*[58] as **Mechanism 4**, with interpretation of evidence that intercalation of both Zn^{2+} and H^+ occurs in Region I, followed by a kinetically slower conversion mechanism in Region II. *Ex situ* XRD, XRF, sXAS, and SEM comparisons of hexagonal *δ*-MnO_2 cycled to the inflection point between Region I and II (1.3 V) and to full discharge (1V) at high (3C) vs. low (C/3) charge rate support this. Full discharge at low rates revealed more substantial conversion products—Mn_3O_4 and $ZnMn_3O_7{\cdot}H_2O$—than the higher charge rates, drawing correlations to the detrimental degradation. The addition of DFT results corroborated their findings, indicating a H^+/Zn^{2+} intercalation reaction to form MnOOH, $Zn_{0.125}MnO_2$, and ZHS each occurred around 1.40 V (Region I plateau). Further discharge reacted these intermediates with additional zinc and H_2O around 1.26V to form final products as Mn_3O_4, MnO, woodruffite, and ZHS.[2]

Whereas MnOOH or $Zn_{0.125}MnO_2$ may share features based on their given parent MnO_2 phases, interstitial site occupation gives rise to more significant structural changes for Zn^{2+} intercalation, thereby justifying the argument for kinetically challenged conversion. That is, phase transformations are expected to be especially sluggish in bulk for the more geometrically and electrochemically stronger Zn^{2+} but may be relatively less constrained near the surface. Analysis of CV curve cathodic/anodic peak polarization and fitting of EIS data provided supporting evidence with respect to kinetics and irreversibility, to be discussed later.[67]

3.1.5 MnO_2 dissolution-deposition follows from solubility of Mn^{2+}, resulting in increased and decreased concentration of aqueous Mn^{2+} in the electrolyte during discharge and charge, respectively. **Mechanism 5** proposed sequential steps during discharge as discussed above: intercalated Zn^{2+} (or H^+) → reduces Mn^{4+} to Mn^{3+} → Mn^{3+} disproportionates to Mn^{4+} and Mn^{2+} → Mn^{2+} dissolves into the aqueous environment. Consequently, in some works that viewed cathode dissolution as undesirable have introduced $MnSO_4$ electrolyte additives to mitigate cathode dissolution.[62] Conversely, other works advocate that the Mn^{2+}/Mn^{4+} transition is the key two-electron electrochemical mechanism for the Zn-MnO_2 system.[5,48,64]

Some debate regarding the presentation of this two-electron reaction as sufficient to account for the entire electrochemical capacity. Two contrasting equations representing reversible dissolution/deposition of the positive electrode are as Eq. 3 or Eq. 4.

$$MnO_2 + 4H^+ + 2e^- \leftrightarrow Mn^{2+} + 2H_2O \quad (3)$$

Eq. 3, as presented by Moon *et al.*,[55] postulates the MnO_2 dissolution may occur even in the mild-acidic electrolyte—as would more typically be expected of highly acidic conditions. Their characterizations indicating no (crystalline) MnOOH or Zn^{2+} intercalated species formed during the initial discharge sequence, and rather amorphous $Zn_\alpha MnO_x$ and woodruffite $[Zn_xMn_3O_7{\cdot}2H_2O]$ began to accumulate throughout later charge/discharge cycles, suggesting the Zn be incorporated into the structures during redeposition of Mn^{2+} upon charging. This in turn leaves the mechanism dominantly dependent upon Mn^{2+} dissolution/deposition on all cycles following the first.

Separate reports provide evidence by detailed characterization of both phase evolution of the cathode species and varying Mn^{2+} concentration in a mild-acid electrolyte.[4,71,72] The corresponding discharge and charge cycles involving dissolution/deposition are presented as Eq. 4:

$$MnO_2 + 2H_2O + 2e^- \leftrightarrow Mn^{2+} + 4OH^- \quad (4)$$

with notable structural evolution. As the tunnel-type pristine cathode material is dissolved in discharge and is redeposited as birnessite [δ-MnO_2] during subsequent charge/discharge cycles—*with* Zn intercalates yet again. Recent *operando* XRF studies—e.g. by Takeuchi *et al*.[5,73]—correlate oxidation state changes with the Mn^{2+} dissolution and deposition throughout charge/discharge cycles and identified redeposited MnO_2 as broken-tunnel α-MnO_2 and Zn-chalcophanite [$ZnMn_3O_7{\cdot}3H_2O$] as charge products. Additional studies have found that such redeposited species to display poor crystallinity, or even amorphous nature, consequently limiting reversibility and capacity.[8,74]

3.1.6 ZHS is persistently involved wherever pH is imbalanced, whether by consumption of H^+ and/or production of OH^-. Equilibrium pH is achieved by the reversible formation of zinc basic salts on the cathode surfaces, as:

$$4Zn^{2+} + 6OH^- + SO_4^{2-} + 5H_2O \rightarrow ZnSO_4[Zn(OH)_2]_3 \cdot 5H_2O \quad (5)$$

ZHS is known to form through a chemical precipitation from Zn^{2+}, SO_4^{2-}, and OH^-, observed in SEM micrographs with EDS, and XRD both *ex situ* and *operando*, but is said to be unstable under the high-energy electron beam of TEM.[3,55,71] Analogous zinc double-layer hydroxide phases form with corresponding anion in the aqueous electrolyte introduced by alternative zinc salts, typically zinc-triflate or zinc-acetate, as discussed in Section 2.4.[46,48,75] In many studies, the intensity of ZHS signals increase and decrease gradually during discharge and charge, respectively.

Whereas ZHS formation has dominantly been considered a coinciding but ultimately passive by-product on the cathode, **Mechanism 6** follows from some recent studies critically investigating ZHS as an active contributor to the system capacity.[44,65,66] Explicitly, correlated exchange of ZHS and aqueous Mn^{2+} for chalcophanite [$ZnMn_3O_7{\cdot}3H_2O$] and solvated $ZnSO_4/Zn^{2+}$ during charge follows Eq. 6:

$$3ZnSO_4[Zn(OH)_2]_3 \cdot 5H_2O + 3Mn^{2+} + 8e^- \leftrightarrow ZnMn_3O_7 \cdot 3H_2O + 3ZnSO_4 + 18OH^- + 8Zn^{2+} + 12H_2O \quad (6)$$

This consideration—with direct contribution to coulombic capacity—is at conflict with the conventionally accepted role of intrinsic but inert byproduct. Nonetheless, the discussion by Stoševski *et al.*[37] regarding the proposed formation of the dual-Mn/Zn variant ZHS [MnZnLDH] provides intriguing ties to

Mechanism 6, with evocative visions of Zn^{2+} and Mn^{2+} exchange in respective layered structures. Modelling works to investigate morphological changes and redox activity for such transformation and interphases of ZHS, MnZnLDH, and chalcophanite may warrant further consideration.

3.2 Degradation Mechanism

Further insights have been presented in numerous studies with interest in detailing the roles of the many aspects of these Zn/MnO_2 battery systems. Various components are presented and discussed to untangle the features evident of good/poor performance and those responsible for degradation. Studies of particle size and shape, for example, indicate significance in morphological details of prepared MnO_2 cathodes and correlated performance.[14,76] Comparison of various manganese-oxide phases, meanwhile, reveal broadly similar electrochemical behaviour, as had been indicated in Figure 5 and discussed in other recent works.[7,8] Discussed among these and the work by Huang *et al.*[2] identify bixbyite α-Mn_2O_3 by Eq. 7

$$\boldsymbol{MnO_2 + 2H^+ + 2e^- \rightarrow Mn_2O_3 + H_2O} \quad (7)$$

Attributing both a conversion reaction induced by H^+ and H^+ insertion to form α-MnOOH to 1.2 V, as in Eq. 2. Such dual-reaction mechanisms may be especially challenging to distinguish properly by *ex situ* analysis. Irreversibility, in their case, then arose from forming spinel phase either each cycle by:

$$\boldsymbol{Zn_xMnO_2 + (0.5 - x)Zn^{2+} + (1 - 2x)e^- \rightarrow 0.5ZnMn_2O_4} \quad (8)$$

Or over the course of 100 cycles:

$$\boldsymbol{Zn_2Mn_3O_8 + Mn^{2+} + 2e^- \rightarrow 2ZnMn_2O_4} \quad (9)$$

by re-integration of dissolved Mn^{2+}. This is in line with *ex situ* micrographs evidence the dissolution and redeposition of cathode materials, evolving from original β-MnO_2 to poorer crystallinity MnO_2, $ZnMn_2O_4$ and ZHS products, as reported by Li *et al.*[77]

Tangentially, *in situ* study by Li *et al.*[54] provided some valuable evidence of competing mechanistic rates of proton intercalation against dissolution/deposition reactions, and exemplify electrolyte engineering to tune the dominant mechanism, in their search for increased capacity retention.

By contrasting intercalation behaviour in high H^+ concentration against H^+ scarce conditions, Zhao *et al.*[68] derived relative rates and specific capacity, motivating the comparison of H^+ migration in MnOOH structures to proton transport in water. They modelled the knocking of nearest neighbour H^+ to propagate continuous transport, as per the Grotthuss proton transport.[68] Such related studies applied critical characterization and modelling techniques in their attempts to thoroughly elucidate the mechanisms at play but are often presented with material comparisons that are atypical, compared to those in Table 2.

Finally, conversion to or deposition of spinel $ZnMn_2O_4$ and woodruffite phases seem insufficiently reversible, per multiple reports of manganese consumption and degrading cell capacity.[6,8,46,55,58,74,78] The presence of multiple Mn^{n+} oxidation states, and tunnels large enough to intercalate fully solvated Zn^{2+}/H_2O all introduce challenges to the accurate characterization of woodruffite.

As debate of the above mechanisms continue in literature, the reversibility of individual reactions is the key factor to achievable capacity and inevitable degradation in AZMOBs. From diligent work and reported characterization, these mechanisms have been greatly elucidated. Throughout Section 3.1, MnO_2 had been discussed ambiguously with respect to polymorph, as these cathode materials have all exhibited performance degradation during cycling, regardless of structures.[7,79] Better understanding of degradation mechanisms, however, entail noting particular polymorphs in this section's discussion.

As discussed above, it is known that MnO_2 cathode materials that intercalate Zn demonstrate complex phase transitions during cycling in aqueous environments, leading to serious capacity fading.[79] Particularly, the tunnel phase of MnO_2 has been expected to follow Eq. 1, of Mechanisms 1 with Zn-ion insertion as follows:

$$\boldsymbol{MnO_2 + xZn^{2+} + 2xe^- \leftrightarrow Zn_xMnO_2} \quad (1)$$

However, many phase transitions have been reported, from the tunnel structures to layered Zn-buserite, Zn-birnessite, spinel $ZnMn_2O_4$, and tunnel phase of Zn_xMnO_2, per Mechanism 4.[22] For example, in spite of the narrow 1 × 1 tunnel, β-MnO_2 phase transitions to the layered Zn-buserite during the initial discharge and subsequently, Zn^{2+} intercalates reversibly into the layered cathode (Figure 7a). The *γ*-MnO_2 also gradually undergoes complex phase transitions. In the early stages of discharge, near-surface *γ*-MnO_2 is converted to spinel $ZnMn_2O_4$. Subsequent Zn^{2+} intercalation through the spinel structure in order to form tunnel *γ*-$Zn_xMn_2O_4$ throughout an intermediate layer, and the layered L- $Zn_xMn_2O_4$ phase is then formed at the core in the final stage (Figure 7b).[75]

The other factor limiting the application of MnO_2 is low electronic conductivity. The MnO_2 also suffers from capacity fading by the poor electronic conductivity that generally give rise to high internal resistance of the active materials.[38] To improve the poor electronic conductivity of MnO_2 cathode materials, the conductive carbonaceous materials such as graphite and carbon fiber paper (CFP) are introduced to form composites with MnO_2.[62] Figure 7c indicates that the composite electrode of MnO_2 and nanostructured carbon decreases the charge-transfer resistance improving electronic conductivity compared to the pristine MnO_2. Note that, the conductivity of cathode also depends on the interface kinetics with electrolyte, Chuai et al., has discovered that by introducing the Poly(vinylpyrrolidone) into aqueous electrolyte, the ion kinetics at electrode-electrolyte interface can be effectively improved.[80]

In addition, MnO_2 cathode materials may undergo serious capacity degradation due to Mn dissolution from active cathode materials during discharge.[5] Figure 7d shows the increase in Mn concentration upon discharge and decreases again upon the charge. Most consequentially, however, some portion of dissolved Mn remains at the fully charged state and thus accumulated in the aqueous electrolyte throughout subsequent cycles. From the incomplete redeposition of the dissolved Mn, it is inferred that the irreversible Mn dissolution from the active

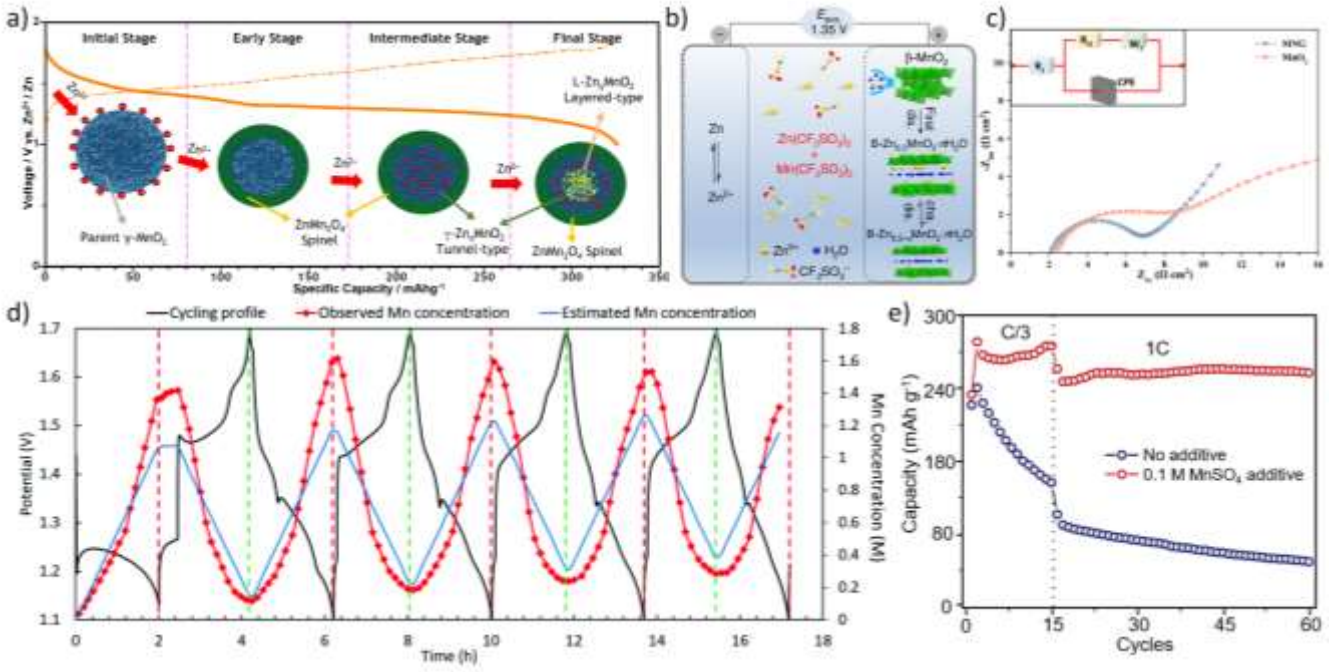

Figure 7 (a) Schematic illustration of the Zn^{2+} intercalation into the tunnel *γ*-MnO_2 cathode. Reproduced with permission.[22] Copyright 2015, American Chemical Society. (b) Schematic illustration of the reaction mechanism of β-MnO2 cathode Reproduced with permission.[75] Copyright 2017 Macmillan Publishers. (c) Nyquist plot of EIS spectra of the pristine δ-MnO_2 and composite of δ-MnO_2 nanoflower/graphite (MNG). Reproduced with permission.[38] Copyright 2017 Nature Publishing group. (d) Mn concentration and Potential curves vs time(h) Reproduced with permission.[5] Copyright 2020 The Royal Society of Chemistry. (e) The cycling performance of MnO2 electrodes with and without 0.1 M $MnSO_4$ additive in a 2 M $ZnSO_4$ aqueous electrolyte at C/3 and 1C, respectively. Reproduced with permission.[3] Copyright 2016 Macmillan Publishers.

materials could be the origin of capacity fading. To relieve this side reaction, the addition of Mn^{2+} salts by the addition of $MnSO_4$ into the aqueous electrolyte suppresses the Mn dissolution and significantly improves cycle performance (Figure 7e).[3]

Additionally, manganese dissolution from MnO_2 is highly dependent on pH and voltage window. Pourbaix diagrams in Figure 3 indicate the promotion of manganese dissolution from MnO_2 in low pH and relevant working voltage (0.3~1.3 V vs. SHE). This manganese dissolution is also closely related to OER near cathode MnO_2. As working conditions begin near the OER border, early stage of discharge have shown abrupt decreases in pH via OER, as seen in Figure 8 and following as:

$$\mathbf{6H_2O \rightarrow O_2(g) + 4H_3O^+(aq) + 4e^-} \quad (12)$$

This OER facilitates the continuous accumulation of H_3O^+ and the pH consequently decreases locally near MnO_2 from ~5 to ~3. In this process, the reduced pH and voltage then promotes manganese dissolution in the aqueous electrolyte, leading to serious capacity fading if irreversible. To relieve this side reaction, many additives (e.g. potassium acetate, $ZnCl_2$, and LiTFSI) suppressing water activity have been reported.[43,81,82] Particularly, sodium dodecyl sulfate [SDS] molecules in aqueous electrolyte were introduced to form a hydrophobic layer on the electrode, preventing water molecules from contacting the electrode to suppress these gas evolution processes.[83] Moreover, to improve the reversibility of MnO_2 dissolution into Mn^{2+}, pH buffer[84] and catalytic additives like Cr^{3+} ions[85] have been introduced to electrolyte for improved cycling life.

Note that low pH of aqueous Zn electrolyte leads to undesirable side reactions with the Zn metal anode. The Pourbaix diagram indicates the electrochemical stability of Zn depending on pH and voltage window (Figure 3). At the mildly acid pH (~5), Zn metal anode in the aqueous Zn electrolyte can exist at the borderline, leading to the oxidation of Zn to Zn^{2+} and the reduction of H^+ to H_2 gas via HER. These two reactions are closely related and promote the corrosion of Zn metal anode following as:

$$\mathbf{Zn(s) \rightarrow Zn^{2+}(aq) + 2e^-} \quad (10)$$

$$\mathbf{2H^+(aq) + 2e^- \rightarrow H_2(g)} \quad (11)$$

The corrosion of Zn metal anode leads to rough surface suppressing the uniform electrochemical kinetics and then degrades cycle and rate performances. The resulting accumulation of H_2 gas in the cell can then lead to cell swelling

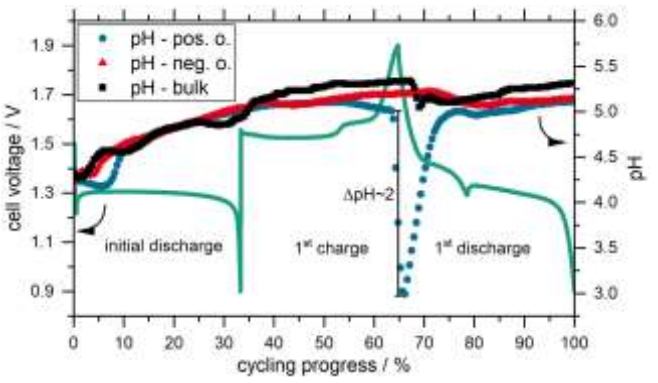

Figure 8 Voltage and pH curve of the AZMOB in the initial discharge and the first cycle. Reproduced with permission.[43] Copyright 2020 Journal of The Electrochemical Society.

and safety hazards. Recently, chemical modification of the Zn metal anode surface is introduced to suppress H_2 gas evolution by increasing the reaction barrier.[86] Since this perspective is focused on manganese oxides cathode, we will not expand the discussion on Zn anode.

4. Perspectives

Practical Areal Capacity and Current Rate Cycling

It is important to note that different reactions in a system exhibit varying degrees of surface sensitivity. For example, Mn dissolution and deposition—as well as ZHS formation and dissolution—are all surface sensitive and occur exclusively on or begin from the surface. In contrast, proton and Zn intercalation and Mn oxide phase conversion are bulk-driven processes. This distinction can lead to differences in battery performance, observations, and conclusions. Surface-sensitive reactions may contribute more than is realistic if the loading areal capacity is low, while bulk-related reactions may be more significant if the areal capacity is high. Similarly, high C-rate battery testing is more related to surface reactions, while lower C-rate testing leads to more bulk reactions, which can contribute to differing system performance under different current rates. In existing literature, high current rates from 3C to 20C have been commonly adopted conditions which pose question regarding the source of stability from surface or bulk regions. Since commercial battery systems must operate at an areal capacity of over 2 mAh cm^{-2} at 1 C or lower current rates, comparative evaluation under these conditions is most relevant to practical applications and to obtain more realistic battery performance.

On the other hand, if Mn deposition—as revealed in recent literature—is an important contributor to the battery capacity, the added Mn salts in the electrolyte will clearly contribute to large capacity which leads to misleading interpretation of cathode materials stability as reported optimizing strategies in existing literature. When the areal capacity is 0.1-1 mAh/cm^2, Mn salts might contribute most of the capacity, obfuscating the stability information of starting cathode through Mn oxide electrodeposition near the end of charging, which would lead to artificially high cycling stability. It is therefore important to present the areal capacity or areal loading in the reports and even more helpful if the volume of electrolyte added can be estimated which can help evaluate the possible contribution of Mn salt on battery capacity. To demonstrate the high stability of optimized Mn-based cathode, it is suggested to use electrolyte without any Mn salt addition or design experiments with and without Mn salt in the electrolyte.

Systematic Study of the Starting Materials

The performance and stability of zinc-ion batteries with manganese dioxide (MnO_2) cathodes depend significantly on the initial materials and their behavior during cycling. During the initial cycling phase, the structure and composition of MnO_2, such as α-Mn_O2 or γ-MnO_2, play crucial roles in determining the battery's capacity and efficiency. However, as the battery cycles—especially after 1st discharge—various transformations can occur, leading to different phases such as spinel $ZnMn_2O_4$ or layered Zn-birnessite. Currently different bodies of literature are using different conditions in materials loading, substrate, current density, voltage range, making the direct comparison very challenging. It is suggested to have a systematic work by evaluating different starting manganese oxides materials and their effects on subsequent phase transition and battery performance under same conditions.

Comprehensive Stability Database of H-Zn-Mn-O-X System with Respect to pH and Voltage

Creating a comprehensive stability database for the H-Zn-Mn-O-X system (where X represents various anions such as sulfate or acetate) is critical. Currently, the database is relatively limited to two or three elements. As we discussed the complexity within this system and the value of the Pourbaix diagram, a more comprehensive diagram considering H and X factors would be highly valuable for practical materials research and design. This database would include data on phase stability under different pH and voltage conditions, providing insights into the behavior of materials during battery operation.

The Phase Transition Pathway

Understanding the phase transition pathways of MnO_2 during charge and discharge cycles is vital for optimizing battery performance. This includes studying how phases like α-MnO_2 convert to other structures such as spinel $ZnMn_2O_4$ or layered Zn-birnessite under different electrochemical conditions, as well as MnO_2 conversion to ZHS or MnO phases. Detailed knowledge of these pathways can help in designing materials to suppress phase transition related materials degradation through structure, alloying or doping strategies.

Optimization Strategies

Due to the evident complexity of this system and the mixed reviews thereof, researchers may put their confidence in particular material phases and respective mechanisms of electrochemistry and degradation. Through further exploration of electrolyte and structural engineering strategies to optimize the improvement to electrochemical performance and mitigation of degradation, further insights will be gained. Supposing dissolution-deposition of Mn^{2+} and the corresponding two-electron reaction is to be optimized, techniques to facilitate maximal reversibility are essential. Such techniques include tuning of the electrolyte with pH buffers[43,84] or catalytic additives,[85] or design of electrode and current collector structures[87] to improve crystallinity of redeposited species. Alternatively, if dissolution-deposition of MnO_x is instead viewed as entirely undesirable, favouring intercalation and/or conversion mechanisms instead, optimization strategies would seek to prevent the Mn^{3+} disproportionation and/or Mn^{2+} dissolution. Approaches may also include tuning of the electrolyte to suppress Mn^{2+} dissolution,[82,83] or augment the cathode material through defect engineering and doping[28,29] or coating.[88–90]

Advanced Characterizations

Due to the complexities of the base system and the added complexities of many potential optimization strategies, thorough characterization approaches are essential. Given the critical role of protons and water molecules in the electrochemical activity of a system, advanced *in situ* and *operando* characterization methods will be especially crucial in clarifying the fundamental mechanisms. *Ex situ* methods typically require drying the sample, which can lead to different observations than those that are true to the aqueous cycling environment, as the evaporation of water molecules can alter the material's structure.[74] A systematic comparison of the characterizations obtained via *ex situ*, *in situ*, and *operando* methods on the same sample or system will provide valuable insights into the impact of characterization methods on observations. The results will not only guide the characterization of Zn-Mn-based aqueous battery, but also shed light on other aqueous battery systems.

The application of *in situ* and *operando* characterizations at practical areal capacity and current rate cycling would provide very powerful insights on the operation mechanism. The results would help the community clarify many puzzles associated with both storage and degradation mechanisms under debate as described in Section 3.

Advanced Multi-scale Materials Modelling

As discussed, intercalation reactions, crystal structure files, oxidation states, thermodynamics, and more are readily available through a long history of experimental-driven modelling. Most of the structures in Figure 1 and Figure 2 followed from The Materials Project.[9] Missing, however, are some complexities introduced by hydrogen and water intercalates, as well as surface-area dependence of non-equilibrium nucleating and crystallization phases requiring more nuanced consideration.[91–93] In an example modelling study for improvement of manganese oxide electrodes, defect-introduced electrodes have been recently designed by density functional theory (DFT) (e.g., SIESTA, Quantum ESPRESSO, VASP, etc.) to tune and understand the thermodynamics of ion insertion.[94] Similarly, recent developments to considerations to excited state physics within or complementary to DFT frameworks are presenting opportunities to model XAS spectra that may eventually be applicable in identifying complex metal oxides cathodes with intercalates or cation deficiency.[95,96] In consideration of solvated ions or molecules and interactions with surfaces, particular schemes may present viable first principles options (VASPsol and JDFTx) with implicit handling of fluids and solvent valuable in application toward aqueous electrolyte/electrode physical chemistry.

Furthermore, certain large systems that may include interactions at interfaces, grain boundaries, and related topologies may be more suited to Molecular Dynamics (MD) approaches with advanced interatomic potentials to better integrate electrochemical physics, or implementation of grand canonical ensemble. In particular, the capabilities of MD (e.g. LAMMPS) to model large systems by implementing interatomic potentials, evolution of the solid electrode interface (SEI) between electrode and electrolyte has been examined.[97] As described, SEI formation is still unclear and is complicated by the high dependency on pH, a dynamic factor in AZMOB systems. Given this, MD approaches could present valuable insights into SEI formation in AZMOBs, with due consideration of pH and potential of the system.

In addition, multiscale approaches have also been utilized to comprehensively examine mechanisms of phase transitions in cathode materials and its effect of the battery performance, e.g. degradation.[98] Multiscale approaches integrate nano-to-macro analysis, drawing thermodynamic properties (e.g. phase barrier and modulus) as calculated by DFT or MD, to use as input parameters in phase transitions, to then be solved via continuum and multiphysics modeling (Abaqus, Ansys, COMSOL, etc.), such as by finite element method (FEM) and finite difference method (FDM). Given the many manganese-based oxide materials and polymorphs outlined in Section 2, and the role of phase transitions in these cathode materials is important to the cathode longevity, as discussed in Section 3. Currently, however, the effect of phase transitions in the AZMOB on the performance has not been fundamentally examined. A multiscale approach examining the underlying mechanism and consequences of phase transitions in the manganese oxide cathode should be undertaken, to provide valuable elucidation.

Characterization/Modelling Integration

Dynamic processes in battery systems, however, rely on these advancing *operando* studies, implementing time-resolved techniques to capture nuanced transformations, where transient meta-stable phases evolve and decay. When such complexities reign, *ab initio* techniques, such as DFT, become essential tools. Exploratory construction and interpolation of various possible permutations between known start/end phases can better elucidate such nuanced mechanisms, *e.g.* by characterizing emergent vibrational modes and electronic states corresponding to birnessite transformation.[26] The practical implementation of *ab initio* calculations must become more prevalent to corroborate *operando* data, to fill gaps in the literature space, and to resolve conflicting reports. Very few studies of Zn-MnO_2 battery systems have been dedicated computational works,[99] though a handful report include synergistic experimental and theoretical data to elucidate mechanisms[58,100–102] or inform mechanisms by consideration of relative MnO_2 stabilities.[91,92] Many forms of *ab initio* modelling can provide powerful tools to focus upon particular mechanisms and phenomena, to provide backing to experimental and theory pulling disparate pieces into a cohesive whole.

Some of the above storage mechanisms arose from supporting computational modelling. Such examples include estimations of reaction kinetics by diffusion barriers[14,68,101] while others consider thermodynamics and formation energy to elucidate redox peaks in CV curves.[58] A select few delve into detailed analysis of charge-transfer and redox behaviour key to the prospective electrochemical mechanisms by detailed study of charge densities, to complement and interpret experimental data such as EELS.[100] Atomistic scale simulations may require significant effort to refine—fitting to experimental (particularly mineralogical) data or high-throughput computing, *i.e.* DFT with data available through www.materialsproject.org.[9] Work to optimize or implement compromises in reasonable representation of electronic vs structural and ionic properties are often necessary. From this data, electrochemists may frame discussion with respect to thermodynamics—as summarized in Pourbiax and phase diagrams,

as in Figure 3—and structural information to better comprehend crystal systems—from .cif or other structure file types, which may be rendered in visualization software.

As advanced *in situ* and *operando* characterization has revealed misunderstandings born of *ex situ* characterization, sophisticated modelling practices should seek to clarify relatively cursory modelling efforts. Bulk crystalline materials and associated intercalation mechanisms are simple and approachable, but surface reaction kinetics require significant attention to detail. Given experimentally noted MnO_2 particle size effects,[76,91,92] we argue that distinguishing surface and bulk mechanisms is of extreme import for the future of this battery system. Correspondingly, conversion reactions may be significantly localized to electrode surface—as examined by STEM-EDS mapping—with greater impact on coulombic capacity and retention than bulk intercalation.[46]

5. Conclusions

While MnO_2 materials make an appealing cathode for safe, energy-dense, and ecologically sourced rechargeable aqueous zinc−metal-oxide batteries, the still-growing body of literature underscores the importance of quality over quantity. With the increased prevalence of *operando* characterization, providing insight into previously conflicting results of *ex situ* studies, several mechanistic explanations have been argued. In consideration of the many stable/meta-stable Zn-Mn-H_2O reaction products, this perspective stresses the need for greater supplementation of *in situ* and *operando* characterizations with modelling work, such as analysis by Density Functional Theory, Molecular Dynamics, and Finite Element Methods. A comprehensive understanding of reaction mechanisms, accounting for pH, voltage windows, diffusion rates, surface reactions, and irreversibility will better inform the ongoing efforts—via electrolyte tuning and cathode structure engineering—to improve longevity and viability in future AZMOBs.

Author Contributions

Matthew Bergschneider and Fantai Kong wrote the manuscript and assembled figures. Taesoon Hwang contributed conceptualization, writing segments, review, figures, and editing to the manuscript. Youhwan Jo, Denyce Alvarez provided valuable and constructive suggestions. Kyeongjae Cho provided project administration and supervision, as well as resources, software, and funding acquisition.

Conflicts of interest

There are no conflicts to declare.

Acknowledgements

The acknowledgements come at the end of an article after the conclusions and before the notes and references.

References

1 J. E. Post, Manganese oxide minerals: Crystal structures and economic and environmental significance, *Proc. Natl. Acad. Sci. U. S. A.*, 1999, **96**, 3447–3454.

2 Y. Huang, J. Mou, W. Liu, X. Wang, L. Dong, F. Kang and C. Xu, Novel Insights into Energy Storage Mechanism of Aqueous Rechargeable Zn/MnO2 Batteries with Participation of Mn2+, *Nano-Micro Lett.*, 2019, **11**, 1–13.

3 H. Pan, Y. Shao, P. Yan, Y. Cheng, K. S. Han, Z. Nie, C. Wang, J. Yang, X. Li, P. Bhattacharya, K. T. Mueller and J. Liu, Reversible aqueous zinc/manganese oxide energy storage from conversion reactions, *Nat. Energy*, 2016, **1**, 1–7.

4 X. Guo, J. Zhou, C. Bai, X. Li, G. Fang and S. Liang, Zn/MnO2 battery chemistry with dissolution-deposition mechanism, *Mater. Today Energy*, 2020, **16**, 100396.

5 D. Wu, L. M. Housel, S. J. Kim, N. Sadique, C. D. Quilty, L. Wu, R. Tappero, S. L. Nicholas, S. Ehrlich, Y. Zhu, A. C. Marschilok, E. S. Takeuchi, D. C. Bock and K. J. Takeuchi, Quantitative temporally and spatially resolved X-ray fluorescence microprobe characterization of the manganese dissolution-deposition mechanism in aqueous Zn/α-MnO2 batteries, *Energy Environ. Sci.*, 2020, **13**, 4322–4333.

6 X. Gao, H. Wu, W. Li, Y. Tian, Y. Zhang, H. Wu, L. Yang, G. Zou, H. Hou and X. Ji, H+-Insertion Boosted α-MnO2 for an Aqueous Zn-Ion Battery, *Small*, 2020, **16**, 1905842.

7 B. Sambandam, V. Mathew, S. Kim, S. Lee, S. Kim, J. Y. Hwang, H. J. Fan and J. Kim, An analysis of the electrochemical mechanism of manganese oxides in aqueous zinc batteries, *Chem*, 2022, **8**, 924–946.

8 U. Siamionau, Y. Aniskevich, A. Mazanik, O. Kokits, G. Ragoisha, J. H. Jo, S. T. Myung and E. Streltsov, Rechargeable zinc-ion batteries with manganese dioxide cathode: How critical is choice of manganese dioxide polymorphs in aqueous solutions?, *J. Power Sources*, 2022, **523**, 231023.

9 A. Jain, S. P. Ong, G. Hautier, W. Chen, W. D. Richards, S. Dacek, S. Cholia, D. Gunter, D. Skinner, G. Ceder and K. A. Persson, Commentary: The Materials Project: A materials genome approach to accelerating materials innovation, *APL Mater.*, 2013, **1**, 011002.

10 K. Momma and F. Izumi, *VESTA 3* for three-dimensional visualization of crystal, volumetric and morphology data, *J. Appl. Crystallogr.*, 2011, **44**, 1272–1276.

11 Y. Chabre and J. Parmetier, Structural and Electrochemical Properties of the Proton / γ-Mn02 System, *Prog. Solid State Chem.*, 1995, **23**, 1–130.

12 Q. Feng, K. Yanagisawa and N. Yamasaki, Hydrothermal Soft Chemical Process for Synthesis of Manganese Oxides with Tunnel Structures, *J. Porous Mater.*, 1998, **18**, 153–161.

13 C. Xu, B. Li, H. Du and F. Kang, Energetic zinc ion chemistry: The rechargeable zinc ion battery, *Angew. Chem. - Int. Ed.*, 2012, **51**, 933–935.

14 K. You, Y. Yuan, X. Liao, W. Song, X. He, H. Jin and S. Wang, Electrochemical Study of Polymorphic MnO2 in Rechargeable Aqueous Zinc Batteries, *Crystals*, 2022, **12**, 1600.

15 X. Sun, C. Ma, Y. Wang and H. Li, Preparation and characterization of MnOOH and β-MnO2 whiskers, *Inorg. Chem. Commun.*, 2002, **5**, 747–750.

16 J. Lee, J. B. Ju, W. I. Cho, B. W. Cho and S. H. Oh, Todorokite-type MnO2 as a zinc-ion intercalating material, *Electrochimica Acta*, 2013, **112**, 138–143.

17 J. E. Post, P. J. Heaney and J. Hanson, Synchrotron X-ray diffraction study of the structure and dehydration behavior of todorokite, *Am. Mineral.*, 2003, **88**, 142–150.
18 M. M. Thackeray, M. H. Rossouw, R. J. Gummow, D. C. Liles, K. Pearce, A. De Kock, W. I. F. David and S. Hulls, Ramsdellite-MnO2 for Lithium Batteries: the Ramsdellite to Spinel Transformation, *Elecrrochimica Acta*, 1993, **38**, 12–1267.
19 J. E. Post and P. J. Heaney, Neutron and X-Ray Study of Ramsdellite and Groutellite, *Am. Mineral.*, 2004, **89**, 969–975.
20 I. Stoševski, A. Bonakdarpour, F. Cuadra and D. P. Wilkinson, Highly crystalline ramsdellite as a cathode material for near-neutral aqueous MnO2/Zn batteries, *Chem. Commun.*, 2019, **55**, 2082–2085.
21 P. M. de Wolff, Interpretation of some γ-MnO 2 diffraction patterns, *Acta Crystallogr.*, 1959, **12**, 341–345.
22 M. H. Alfaruqi, V. Mathew, J. Gim, S. Kim, J. Song, J. P. Baboo, S. H. Choi and J. Kim, Electrochemically induced structural transformation in a γ-MnO2 cathode of a high capacity zinc-ion battery system, *Chem. Mater.*, 2015, **27**, 3609–3620.
23 L. Huang, X. Luo, C. Chen and Q. Jiang, A high specific capacity aqueous zinc-manganese battery with a ε-MnO2 cathode, *Ionics*, 2021, **27**, 3933–3941.
24 E. A. Johnson and J. E. Post, Water in the interlayer region of birnessite: Importance in cation exchange and structural stability, *Am. Mineral.*, 2006, **91**, 609–618.
25 B. Lee, H. R. Lee, H. Kim, K. Y. Chung, B. W. Cho and S. H. Oh, Elucidating the intercalation mechanism of zinc ions into α-MnO2 for rechargeable zinc batteries, *Chem. Commun.*, 2015, **51**, 9265–9268.
26 F. T. Ling, J. E. Post, P. J. Heaney, J. D. Kubicki and C. M. Santelli, Fourier-transform infrared spectroscopy (FTIR) analysis of triclinic and hexagonal birnessites, *Spectrochim. Acta - Part Mol. Biomol. Spectrosc.*, 2017, **178**, 32–46.
27 J. E. Post, P. J. Heaney and Y. Cho, Neutron diffraction study of hydrogen in birnessite structures, *Am. Mineral.*, 2011, **96**, 534–540.
28 Y. Ding, W. Xue, K. Chen, C. Yang, Q. Feng, D. Zheng, W. Xu, F. Wang and X. Lu, Sodium Ion Pre-Intercalation of δ-MnO2 Nanosheets for High Energy Density Aqueous Zinc-Ion Batteries, *Nanomaterials*, 2023, **13**, 1075.
29 G. Wang, Y. Wang, B. Guan, J. Liu, Y. Zhang, X. Shi, C. Tang, G. Li, Y. Li, X. Wang and L. Li, Hierarchical K-Birnessite-MnO2 Carbon Framework for High-Energy-Density and Durable Aqueous Zinc-Ion Battery, *Small*, 2021, **17**, 2104557.
30 C. Yuan, Y. Zhang, Y. Pan, X. Liu, G. Wang and D. Cao, Investigation of the intercalation of polyvalent cations (Mg2+, Zn2+) into λ-MnO2 for rechargeable aqueous battery, *Electrochimica Acta*, 2014, **116**, 404–412.
31 S. Turner and J. E. Post, Refinement of the substructure and superstructure of romanechite, *Am. Mineral.*, 1988, **7**, 1155–1161.
32 Y. Liu, J. Yao, J. Jiang, Y. Li and Q. Zhu, Exploring the effect of different additives on the preparation of α-Mn2O3/Mn3O4 composites and their zinc ion storage performances, *Ionics*, 2023, **29**, 1469–1478.
33 J. Wang, J. G. Wang, H. Liu, Z. You, C. Wei and F. Kang, Electrochemical activation of commercial MnO microsized particles for high-performance aqueous zinc-ion batteries, *J. Power Sources*, 2019, **438**, 226951.
34 B. Lee, C. S. Yoon, H. R. Lee, K. Y. Chung, B. W. Cho and S. H. Oh, Electrochemically-induced reversible transition from the tunneled to layered polymorphs of manganese dioxide, *Sci. Rep.*, 2014, **4**, 1–8.
35 W. Gou, H. Chen, Z. Xu, Yi. Sun, X. Han, M. Liu and Y. Zhang, High Specific Capacity and Mechanism of a Metal-organic Framework Based Cathode for Aqueous Zinc-ion Batteries, *Energy Adv.*, 2022, **1**, 1065–1070.
36 J. E. Post and P. J. Heaney, Time-resolved synchrotron X-ray diffraction study of the dehydration behavior of chalcophanite, *Am. Mineral.*, 2014, **99**, 1956–1961.
37 I. Stoševski, A. Bonakdarpour, B. Fang, P. Lo and D. P. Wilkinson, Formation of MnxZny(OH)zSO4·5H2O – not intercalation of Zn – is the basis of the neutral MnO2/Zn battery first discharge reaction, *Electrochimica Acta*, 2021, **390**, 2001595.
38 S. Khamsanga, R. Pornprasertsuk, T. Yonezawa, A. A. Mohamad and S. Kheawhom, δ-MnO2 nanoflower/graphite cathode for rechargeable aqueous zinc ion batteries, *Sci. Rep.*, 2019, **9**, 1–9.
39 A. D. Wadsley, Interstitial Atoms in the Layer Structure ZnMn3O7.3H20 (Chalcophanite), *Boldingh J Rec Trav Chim*, 1953, **172**, 1103–1104.
40 A. D. Wadsley, The Crystal Structure of Chalcophanite, ZnMn3O7. 3H20, *Acta Cryst*, 1955, **8**, 165.
41 J. E. Post and D. E. Appleman, Chalcophanite, ZnMn3O7.3H2O: New crystal-structure determinations, *Am. Mineral.*, 1988, **73**, 1401–1404.
42 J. E. Post, P. J. Heaney, C. L. Cahill and L. W. Finger, Woodruffite: A new Mn oxide structure with 3 × 4 tunnels, *Am. Mineral.*, 2003, **88**, 1697–1702.
43 C. F. Bischoff, O. S. Fitz, J. Burns, M. Bauer, H. Gentischer, K. P. Birke, H.-M. Henning and D. Biro, Revealing the Local pH Value Changes of Acidic Aqueous Zinc Ion Batteries with a Manganese Dioxide Electrode during Cycling, *J. Electrochem. Soc.*, 2020, **167**, 020545.
44 H. Chen, C. Dai, F. Xiao, Q. Yang, S. Cai, M. Xu, H. J. Fan and S. J. Bao, Reunderstanding the Reaction Mechanism of Aqueous Zn–Mn Batteries with Sulfate Electrolytes: Role of the Zinc Sulfate Hydroxide, *Adv. Mater.*, 2022, **34**, 2109092.
45 R. K. Rastsvetaeva, S. M. Aksenov, N. V. Chukanov and I. A. Verin, Crystal structure of a new mineral lahnsteinite Zn4(SO4)(OH)6.3H2O, *Crystallogr. Rep.*, 2012, **57**, 737–741.
46 S. J. Kim, D. Wu, L. M. Housel, L. Wu, K. J. Takeuchi, A. C. Marschilok, E. S. Takeuchi and Y. Zhu, Toward the Understanding of the Reaction Mechanism of Zn/MnO2 Batteries Using Non-alkaline Aqueous Electrolytes, *Chem. Mater.*, 2021, **33**, 7283–7289.
47 L. Schlur, A. Carton and G. Pourroy, A new zinc hydroxy acetate hydrogen carbonate lamellar phase for growing large and clean ZnO nanorod arrays, *Chem. Commun.*, 2015, **51**, 3367–3370.
48 D. Wu, L. M. Housel, S. T. King, Z. R. Mansley, N. Sadique, Y. Zhu, L. Ma, S. N. Ehrlich, H. Zhong, E. S. Takeuchi, A. C. Marschilok, D. C. Bock, L. Wang and K. J. Takeuchi, Simultaneous Elucidation of Solid and Solution Manganese Environments via Multiphase Operando Extended X-ray Absorption Fine Structure Spectroscopy in Aqueous Zn/MnO2 Batteries, *J. Am. Chem. Soc.*, 2022, **144**, 23405–23420.
49 J. H. Jo, Y. Aniskevich, J. Kim, J. U. Choi, H. J. Kim, Y. H. Jung, D. Ahn, T. Y. Jeon, K. S. Lee, S. H. Song, H. Kim, G. Ragoisha, A. Mazanik, E. Streltsov and S. T. Myung, New Insight on Open-Structured Sodium Vanadium Oxide as High-Capacity and Long Life Cathode for Zn–Ion Storage: Structure, Electrochemistry, and First-Principles Calculation, *Adv. Energy Mater.*, 2020, **10**, 2001595.

50 J. Wang, Y. C. K. Chen-Wiegart and J. Wang, In operando tracking phase transformation evolution of lithium iron phosphate with hard X-ray microscopy, *Nat. Commun.*, 2014, **5**, 4570.
51 Y. Xu, E. Hu, K. Zhang, X. Wang, V. Borzenets, Z. Sun, P. Pianetta, X. Yu, Y. Liu, X. Q. Yang and H. Li, In situ Visualization of State-of-Charge Heterogeneity within a LiCoO2 Particle that Evolves upon Cycling at Different Rates, *ACS Energy Lett.*, 2017, **2**, 1240–1245.
52 J. E. Post, D. A. McKeown and P. J. Heaney, Raman spectroscopy study of manganese oxides: Tunnel structures, *Am. Mineral.*, 2020, **105**, 1175–1190.
53 E. S. Ilton, J. E. Post, P. J. Heaney, F. T. Ling and S. N. Kerisit, XPS determination of Mn oxidation states in Mn (hydr)oxides, *Appl. Surf. Sci.*, 2016, **366**, 475–485.
54 X. Li, Z. Xu, Y. Qian and Z. Hou, In-situ regulated competitive proton intercalation and deposition/dissolution reaction of MnO2 for high-performance flexible zinc-manganese batteries, *Energy Storage Mater.*, 2022, **53**, 72–78.
55 H. Moon, K. H. Ha, Y. Park, J. Lee, M. S. Kwon, J. Lim, M. H. Lee, D. H. Kim, J. H. Choi, J. H. Choi and K. T. Lee, Direct Proof of the Reversible Dissolution/Deposition of Mn2+/Mn4+ for Mild-Acid Zn-MnO2 Batteries with Porous Carbon Interlayers, *Adv. Sci.*, 2021, **8**, 2003714.
56 A. Moezzi, M. B. Cortie and A. M. McDonagh, Zinc hydroxide sulphate and its transformation to crystalline zinc oxide, *Dalton Trans.*, 2013, **42**, 14432–14437.
57 C. Li, S. Jin, L. A. Archer and L. F. Nazar, Toward practical aqueous zinc-ion batteries for electrochemical energy storage, *Joule*, 2022, **6**, 1733–1738.
58 Y. Li, S. Wang, J. R. Salvador, J. Wu, B. Liu, W. Yang, J. Yang, W. Zhang, J. Liu and J. Yang, Reaction Mechanisms for Long-Life Rechargeable Zn/MnO2 Batteries, *Chem. Mater.*, 2019, **31**, 2036–2047.
59 S. Islam, M. H. Alfaruqi, V. Mathew, J. Song, S. Kim, S. Kim, J. Jo, J. P. Baboo, D. T. Pham, D. Y. Putro, Y. K. Sun and J. Kim, Facile synthesis and the exploration of the zinc storage mechanism of β-MnO2 nanorods with exposed (101) planes as a novel cathode material for high performance eco-friendly zinc-ion batteries, *J. Mater. Chem. A*, 2017, **5**, 23299–23309.
60 C. Xu, H. Du, B. Li, F. Kang and Y. Zeng, Reversible insertion properties of zinc ion into manganese dioxide and its application for energy storage, *Electrochem. Solid-State Lett.*, 2009, **12**, A61–A65.
61 P. Oberholzer, E. Tervoort, A. Bouzid, A. Pasquarello and D. Kundu, Oxide versus Nonoxide Cathode Materials for Aqueous Zn Batteries: An Insight into the Charge Storage Mechanism and Consequences Thereof, *ACS Appl. Mater. Interfaces*, 2019, **11**, 674–682.
62 W. Sun, F. Wang, S. Hou, C. Yang, X. Fan, Z. Ma, T. Gao, F. Han, R. Hu, M. Zhu and C. Wang, Zn/MnO2 Battery Chemistry with H+ and Zn2+ Coinsertion, *J. Am. Chem. Soc.*, 2017, **139**, 9775–9778.
63 W. Liu, X. Zhang, Y. Huang, B. Jiang, Z. Chang, C. Xu and F. Kang, β-MnO2 with proton conversion mechanism in rechargeable zinc ion battery, *J. Energy Chem.*, 2021, **56**, 365–373.
64 Z. Liu, L. Qin, B. Lu, X. Wu, S. Liang and J. Zhou, Issues and Opportunities Facing Aqueous Mn2+/MnO2-based Batteries, *ChemSusChem*, 2022, **15**, e202200348.
65 L. Godeffroy, I. Aguilar, J. Médard, D. Larcher, J. M. Tarascon and F. Kanoufi, Decoupling the Dynamics of Zinc Hydroxide Sulfate Precipitation/Dissolution in Aqueous Zn–MnO2 Batteries by Operando Optical Microscopy: A Missing Piece of the Mechanistic Puzzle, *Adv. Energy Mater.*, 2022, **12**, 2200722.
66 B. Lee, J. Choi, M. Lee, S. Han, M. Jeong, T. Yim and S. H. Oh, Unraveling the critical role of Zn-phyllomanganates in zinc ion batteries, *J. Mater. Chem. A*, 2021, **9**, 13950–13957.
67 S. W. Donne, G. A. Lawrance and D. A. J. Swinkels, Redox Processes at the Manganese Dioxide Electrode: II. Slow-Scan Cyclic Voltammetry, *J Electrochem Soc*, 1997, **144**, 2954.
68 Q. Zhao, A. Song, W. Zhao, R. Qin, S. Ding, X. Chen, Y. Song, L. Yang, H. Lin, S. Li and F. Pan, Boosting the Energy Density of Aqueous Batteries via Facile Grotthuss Proton Transport, *Angew. Chem. - Int. Ed.*, 2021, **60**, 4169–4174.
69 C. A. Marianetti, G. Ceder and D. Morgan, First-principles investigation of the cooperative Jahn-Teller effect for octahedrally coordinated transition-metal ions, *Phys. Rev. B - Condens. Matter Mater. Phys.*, 2001, **63**, 1–15.
70 M. D. Radin and A. Van Der Ven, Simulating Charge, Spin, and Orbital Ordering: Application to Jahn-Teller Distortions in Layered Transition-Metal Oxides, *Chem. Mater.*, 2018, **30**, 607–618.
71 B. Lee, H. R. Seo, H. R. Lee, C. S. Yoon, J. H. Kim, K. Y. Chung, B. W. Cho and S. H. Oh, Critical Role of pH Evolution of Electrolyte in the Reaction Mechanism for Rechargeable Zinc Batteries, *ChemSusChem*, 2016, **9**, 2948–2956.
72 X. Shen, X. Wang, Y. Zhou, Y. Shi, L. Zhao, H. Jin, J. Di and Q. Li, Highly Reversible Aqueous Zn-MnO2 Battery by Supplementing Mn2+-Mediated MnO2 Deposition and Dissolution, *Adv. Funct. Mater.*, 2021, **31**, 2101579.
73 S. J. Kim, D. Wu, N. Sadique, C. D. Quilty, L. Wu, A. C. Marschilok, K. J. Takeuchi, E. S. Takeuchi and Y. Zhu, Unraveling the Dissolution-Mediated Reaction Mechanism of α-MnO2 Cathodes for Aqueous Zn-Ion Batteries, *Small*, 2020, **16**, 2005406.
74 V. R. Kankanallu, X. Zheng, D. Leschev, N. Zmich, C. Clark, C.-H. Lin, H. Zhong, S. Ghose, A. M. Kiss, D. Nykypanchuk, E. Stavitski, E. S. Takeuchi, A. C. Marschilok, K. J. Takeuchi, J. Bai, M. Ge and Y. K. Chen-Wiegart, Elucidating a dissolution–deposition reaction mechanism by multimodal synchrotron X-ray characterization in aqueous Zn/MnO2 batteries, *Energy Environ. Sci.*, 2023, **16**, 2464–2482.
75 N. Zhang, F. Cheng, J. Liu, L. Wang, X. Long, X. Liu, F. Li and J. Chen, Rechargeable aqueous zinc-manganese dioxide batteries with high energy and power densities, *Nat. Commun.*, 2017, **8**, 1–9.
76 Z. Tang, W. Chen, Z. Lyu and Q. Chen, Size-Dependent Reaction Mechanism of λ-MnO2 Particles as Cathodes in Aqueous Zinc-Ion Batteries, *Energy Mater. Adv.*, 2022, **2022**, 9765710.
77 L. Li, T. K. A. Hoang, J. Zhi, M. Han, S. Li and P. Chen, Functioning Mechanism of the Secondary Aqueous Zn-β-MnO2 Battery, *ACS Appl. Mater. Interfaces*, 2020, **12**, 12834–12846.
78 S. Zhao, B. Han, D. Zhang, Q. Huang, L. Xiao, L. Chen, D. G. Ivey, Y. Deng and W. Wei, Unravelling the reaction chemistry and degradation mechanism in aqueous Zn/MnO2 rechargeable batteries, *J. Mater. Chem. A*, 2018, **6**, 5733–5739.
79 N. Zhang, X. Chen, M. Yu, Z. Niu, F. Cheng and J. Chen, Materials chemistry for rechargeable zinc-ion batteries, *Chem. Soc. Rev.*, 2020, **49**, 4203–4219.
80 M. Chuai, J. Yang, R. Tan, Z. Liu, Y. Yuan, Y. Xu, J. Sun, M. Wang, X. Zheng, N. Chen and W. Chen, Theory-Driven Design of a Cationic Accelerator for High-Performance Electrolytic MnO2–Zn Batteries, *Adv. Mater.*, 2022, **34**, 2203249.
81 V. Verma, S. Kumar, W. Manalastas and M. Srinivasan, Undesired Reactions in Aqueous Rechargeable Zinc Ion Batteries, *ACS Energy Lett.*, 2021, **6**, 1773–1785.
82 S. Liu, J. Mao, W. K. Pang, J. Vongsvivut, X. Zeng, L. Thomsen, Y. Wang, J. Liu, D. Li and Z. Guo, Tuning the Electrolyte Solvation Structure to Suppress Cathode Dissolution, Water Reactivity, and

Zn Dendrite Growth in Zinc-Ion Batteries, *Adv. Funct. Mater.*, 2021, **31**, 2104281.

83 H. Guo, Z. Shao, Y. Zhang, X. Cui, L. Mao, S. Cheng, M. Ma, W. Lan, Q. Su and E. Xie, Electrolyte additives inhibit the surface reaction of aqueous sodium/zinc battery, *J. Colloid Interface Sci.*, 2022, **608**, 1481–1488.

84 Z. Liu, Y. Yang, S. Liang, B. Lu and J. Zhou, pH-Buffer Contained Electrolyte for Self-Adjusted Cathode-Free Zn–MnO 2 Batteries with Coexistence of Dual Mechanisms, *Small Struct.*, 2021, **2**, 2100119.

85 Z. Liu, Y. Yang, B. Lu, S. Liang, H. J. Fan and J. Zhou, Insights into complexing effects in acetate-based Zn-MnO2 batteries and performance enhancement by all-round strategies, *Energy Storage Mater.*, 2022, **52**, 104–110.

86 P. Xiao, H. Li, J. Fu, C. Zeng, Y. Zhao, T. Zhai and H. Li, An anticorrosive zinc metal anode with ultra-long cycle life over one year, *Energy Environ. Sci.*, 2022, **15**, 1638–1646.

87 Z. Shen, Y. Liu, L. Luo, J. Pu, Y. Ji, J. Xie, L. Li, C. Li, Y. Yao and G. Hong, Interface Engineering of Aqueous Zinc/Manganese Dioxide Batteries with High Areal Capacity and Energy Density, *Small*, , DOI:10.1002/smll.202204683.

88 S. Le, B. Yan, Y. Mao, D. Chi, M. Zhu, H. Jia, G. Zhao, X. Zhu and N. Zhang, N-doped δ-MnO2 coated N-doped carbon cloth as stable cathode for aqueous zinc-ion batteries, *Int. J. Electrochem. Sci.*, 2023, **18**, 1–8.

89 H. Chen, J. Guo, S. Tan, X. Zhang, Z. Sang and D. Yang, Dual-modification of oxygen vacancies and PEDOT coating on MnO2 nanowires for high-performance zinc ion battery, *Appl. Surf. Sci.*, 2023, **638**, 158057.

90 L. Wang, X. Wang, B. Song, Z. Wang, L. Zhang and Q. Lu, Facile in situ synthesis of PEDOT conductor interface at the surface of MnO2 cathodes for enhanced aqueous zinc-ion batteries, *Surf. Interfaces*, 2022, **33**, 102222.

91 B. R. Chen, W. Sun, D. A. Kitchaev, J. S. Mangum, V. Thampy, L. M. Garten, D. S. Ginley, B. P. Gorman, K. H. Stone, G. Ceder, M. F. Toney and L. T. Schelhas, Understanding crystallization pathways leading to manganese oxide polymorph formation, *Nat. Commun.*, 2018, **9**, 2553.

92 W. Sun, D. A. Kitchaev, D. Kramer and G. Ceder, Non-equilibrium crystallization pathways of manganese oxides in aqueous solution, *Nat. Commun.*, 2019, **10**, 573.

93 D. A. Kitchaev, H. Peng, Y. Liu, J. Sun, J. P. Perdew and G. Ceder, Energetics of MnO2 polymorphs in density functional theory, *Phys. Rev. B*, 2016, **93**, 1–5.

94 M. Han, J. Huang, S. Liang, L. Shan, X. Xie, Z. Yi, Y. Wang, S. Guo and J. Zhou, Oxygen Defects in β-MnO2 Enabling High-Performance Rechargeable Aqueous Zinc/Manganese Dioxide Battery, *iScience*, 2020, **23**, 100797.

95 T. A. Pascal, U. Boesenberg, R. Kostecki, T. J. Richardson, T.-C. Weng, D. Sokaras, D. Nordlund, E. McDermott, A. Moewes, J. Cabana and D. Prendergast, Finite temperature effects on the X-ray absorption spectra of lithium compounds: First-principles interpretation of X-ray Raman measurements, *J. Chem. Phys.*, 2014, **140**, 034107.

96 A. Sanz-Matias, S. Roychoudhury, X. Feng, F. Yang, L. C. Kao, K. R. Zavadil, J. Guo and D. Prendergast, Excitonic Effects in X-ray Absorption Spectra of Fluoride Salts and Their Surfaces, *Chem. Mater.*, 2022, **34**, 9144–9158.

97 V. Ponce, D. E. Galvez-Aranda and J. M. Seminario, Analysis of a Li-Ion Nanobattery with Graphite Anode Using Molecular Dynamics Simulations, *J. Phys. Chem. C*, 2017, **121**, 12959–12971.

98 J. M. Lim, T. Hwang, D. Kim, M. S. Park, K. Cho and M. Cho, Intrinsic Origins of Crack Generation in Ni-rich LiNi0.8Co0.1Mn0.1O2 Layered Oxide Cathode Material, *Sci. Rep.*, 2017, **7**, 39669.

99 C. Xu, Y. Chen, S. Shi, J. Li, F. Kang and D. Su, Secondary batteries with multivalent ions for energy storage, *Sci. Rep.*, 2015, **5**, 14120.

100 D. Chao, W. Zhou, C. Ye, Q. Zhang, Y. Chen, L. Gu, K. Davey and S. Qiao, An Electrolytic Zn–MnO2 Battery for High-Voltage and Scalable Energy Storage, *Angew. Chem.*, 2019, **131**, 7905–7910.

101 X. Huang, X. Liu, H. Li, Q. Zhao and T. Ma, Revealing the Real Charge Carrier in Aqueous Zinc Batteries Based on Polythiophene/Manganese Dioxide Cathode, *Small Struct.*, 2022, 2200221.

102 T. Le, N. Sadique, L. M. Housel, A. S. Poyraz, E. S. Takeuchi, K. J. Takeuchi, A. C. Marschilok and P. Liu, Discharging Behavior of Hollandite α-MnO2 in a Hydrated Zinc-Ion Battery, *ACS Appl. Mater. Interfaces*, 2021, **13**, 59937–59949.

Data Availability Statement

No additional data, software, or code outside of cited work was essential to this work.